2020

Geochemical Constraints on Mantle Sources and Basalt Petrogenesis in the Strait of Sicily Rift Zone (Italy): Insights into the Importance of Short Lengthscale Mantle Heterogeneity.

John C. White
Eastern Kentucky University, john.white@eku.edu

David A. Neave
University of Manchester

Silvio G. Rotolo
University of Palermo

Don F. Parker
Baylor University

Recommended Citation

Geochemical constraints on basalt petrogenesis in the Strait of Sicily Rift Zone (Italy): Insights into the importance of short lengthscale mantle heterogeneity

John Charles White[a,*], David A. Neave[b], Silvio G. Rotolo[c,d], Don F. Parker[e,1]

[a] *Department of Geosciences, Eastern Kentucky University, 521 Lancaster Ave., Science 2234, Richmond, KY 40475, USA*
[b] *Department of Earth and Environmental Sciences, The University of Manchester, Oxford Road, Manchester M13 9PL, United Kingdom*
[c] *Dipartimento di Scienze della Terra e del Mare (DiSTeM), Università di Palermo, Via Archirafi 36, 90123 Palermo, Italy*
[d] *Instituto Nazionale di Geofisica e Vulcanologia (INGV), Sezione di Palermo, Via Ugo La Malfa 153, 90146 Palermo, Italy*
[e] *Department of Geosciences, Baylor University, Waco, TX 76798, USA*

ABSTRACT

Igneous activity from the late Miocene to historic time (most recently 1891 CE) in the Strait of Sicily has created two volcanic islands (Pantelleria and Linosa) and several seamounts. These volcanoes are dominated by transitional (ol + hy-normative) to alkaline (ne-normative) basaltic lavas and scoriae; volcanic felsic rocks (peralkaline trachyte-rhyolite) crop out only on Pantelleria. Although most likely erupted through continental crust, basalts demonstrate no evidence of crustal contamination and are geochemically similar to oceanic island basalts (OIB). Despite their isotopic similarities, there are considerable compositional differences with respect to major and trace element geochemistry both between and within the two islands that are due to short-length scale mantle heterogeneity beneath the region as well as variability in partial melting and magma storage conditions. Published geophysical surveys suggest that lithospheric thickness beneath both islands is ~60 km; this is consistent with the results of our geochemical modelling (59–60 km), which also suggest mantle potential temperatures between 1415 and 1435 ˚C, similar to those documented in other continental passive rifts. Trace element and isotopic data reveal that the asthenosphere beneath the Strait of Sicily is heterogenous at both inter-island (100s of km) and intra-island (10s of km) scales. Although there is some compositional overlap between the two major synthems at Linosa, in general the older magmas (Arena Bianca, 700 ka) formed as a result of ~5% partial melting of a depleted MORB mantle (DMM) source enriched with a relatively small amount of recycled MORB material, whereas the younger magmas (Monte Bandiera, 530 ka) formed as a result of ~2% partial melting of a similar mantle source. Pantelleria magmas formed from a higher degree (~6%) of partial melting of a DMM source with a relatively greater amount of recycled MORB material and possibly other components. Geochemical modelling also suggests the older magmas on Linosa differentiated at a much shallower level (~8 km) than the younger magmas (~25 km, at or below the base of the crust) prior to eruption. Magmas stored in higher-level reservoirs were effectively homogenized and preserve a narrower compositional range than magmas sourced from depth. Data for the seamounts are scarce and compromised by significant seawater alteration; thus, these volcanic centers cannot be modelled but based on comparative geochemistry with the islands are likely the result of even smaller (< 2%) degrees of partial melting beneath thicker (> 60 km) lithosphere. Despite the geophysical similarities between the two islands in terms of lithospheric thickness and crustal thinning, melt productivity has been greater at Pantelleria, producing a much larger island and sustaining felsic magmatism, which we hypothesize may ultimately be entirely due to the local occurrence of much more fusible mantle.

* Corresponding author.
  E-mail address: john.white@eku.edu (J.C. White).
[1] School of Math and Science, Wayland Baptist University, 1900 West 7th Street, Plainview, TX 79072, USA.

1. Introduction

The Mediterranean Sea between the island of Sicily and the Tunisian coast is the setting for magmatism with an Oceanic Island Basalt (OIB)-like affinity that has produced two islands (Pantelleria and Linosa) and several seamounts that occur subparallel to the faulted margins of two of the three northwest-southeast trending grabens that comprise the Strait of Sicily Rift Zone (SSRZ; Fig. 1). Transitional (hy + ol-normative) to alkali (ne-normative) basaltic lavas and tuffs occur throughout the SSRZ, with evolved lavas and tuffs (peralkaline trachyte and rhyolite [pantellerite]) cropping out only at Pantelleria, where they form a bimodal association typical of intraplate magmatic settings (Mahood and Hildreth, 1986; Civetta et al., 1998; Bindi et al., 2002; Rotolo et al., 2006; Di Bella et al., 2008; White et al., 2009; Neave et al., 2012; Avanzinelli et al., 2014).

Geochemical studies have revealed that the mantle source for the SSRZ is almost isotopically homogenous: basalts throughout the rift zone have nearly identical $^{87}Sr/^{86}Sr$ ratios (Linosa: 0.7031 ± 0.0001; Pantelleria: 0.7032 ± 0.0001; Seamounts: 0.7035 ± 0.0005) and very similar $^{143}Nd/^{144}Nd$ ratios (Linosa: 0.51291–0.51297 [ε_{Nd} = 5.9 ± 0.5]; Pantelleria: 0.51287–0.51299 [ε_{Nd} = 6.3 ± 0.5]; Seamounts: 0.51299–0.51312 [ε_{Nd} = 7.7 ± 0.5]) (Esperança and Crisci, 1995; Civetta et al., 1998; Rotolo et al., 2006; Di Bella et al., 2008; Avanzinelli et al., 2014). Helium isotopes recorded at both Pantelleria and Linosa are also similar ($^{3}He/^{4}He$ = 7.3–7.6 R/R$_a$, Parello et al., 2000; Fouré et al., 2012) and MORB-like (8 ± 1 R/R$_a$, Class and Goldstein, 2005). Intra- and inter-island lead isotope ratio variations are larger, becoming more radiogenic from the older Linosa suite (1070 to 530 ka, $^{206}Pb/^{204}Pb$ = 19.320–19.540) to the paleo-Pantelleria suite (120–80 ka, $^{206}Pb/^{204}Pb$ = 19.664–19.981), with the younger (29–10 ka) neo-Pantelleria suite showing intermediate values ($^{206}Pb/^{204}Pb$ = 19.445–19.791, Avanzinelli et al., 2014) and the Seamounts having a range that overlaps all of these ($^{206}Pb/^{204}Pb$ = 19.153–19.693, Rotolo et al., 2006). These isotopic data place the Pantelleria and Linosa basalts on the Sr-Nd mantle array between depleted MORB mantle (DMM) and primitive mantle (PM),

where they plot with OIB. On Sr-Nd-Pb diagrams they plot in the compositional space assigned to "Prevalent Mantle" (PREMA) (Zindler and Hart, 1986; Stracke, 2012). These results have been used to support diverse interpretations for the source origin of basaltic magmatism in the SSRZ: (1) lithospheric mantle chemically modified by the addition of recycled MORB material (Esperança and Crisci, 1995); (2) depleted MORB mantle enriched by a fossil plume of deep mantle material (Civetta et al., 1998; Rotolo et al., 2006); (3) a mixture of asthenospheric and metasomatized lithospheric mantle (Di Bella et al., 2008); and (4) asthenosphere enriched with an eclogitic component representing recycled MORB material (Avanzinelli et al., 2014). In this latter study, Avanzinelli et al. (2014) included the results of U-series disequilibrium systematics for the neo-Pantelleria lavas and concluded that the sources for these are strictly asthenospheric with no need for interaction with lithospheric mantle or continental crust nor any need for a metasomatic component, thus ruling out hypotheses (1) and (3) listed above.

Unlike their isotopic ratios, the major and trace element geochemistry of the basalts demonstrates considerable variability. At Pantelleria, Civetta et al. (1998) divided the basalts into "High Ti-P" and "Low Ti-P" types, with the former also characterized by higher concentrations of incompatible trace elements and higher LREE/HREE than the latter, which they attributed to different degrees of partial melting from a locally heterogeneous asthenospheric mantle (cf. Mahood and Baker, 1986). Similar differences were described on Linosa, where Di Bella et al. (2008) recognized a "Trend-A" and "Trend-B", with the former having higher K$_2$O, P$_2$O$_5$, incompatible trace elements (e.g., Rb, Th), and LREE/HREE at a given MgO. Although Di Bella et al. (2008) attributed the differences between the volcanic centers of the SSRZ to varying degrees of partial melting from heterogeneous mantle sources, they modelled the Linosa trends as differentiates from a common primary magma (their hypothetical "Trend-C").

Several methods have been proposed to constrain mantle source compositions and partial melting parameters using major and trace element geochemistry. The first goal of this paper is to compare the results of some of these methods, including: (1) the use of olivine-liquid
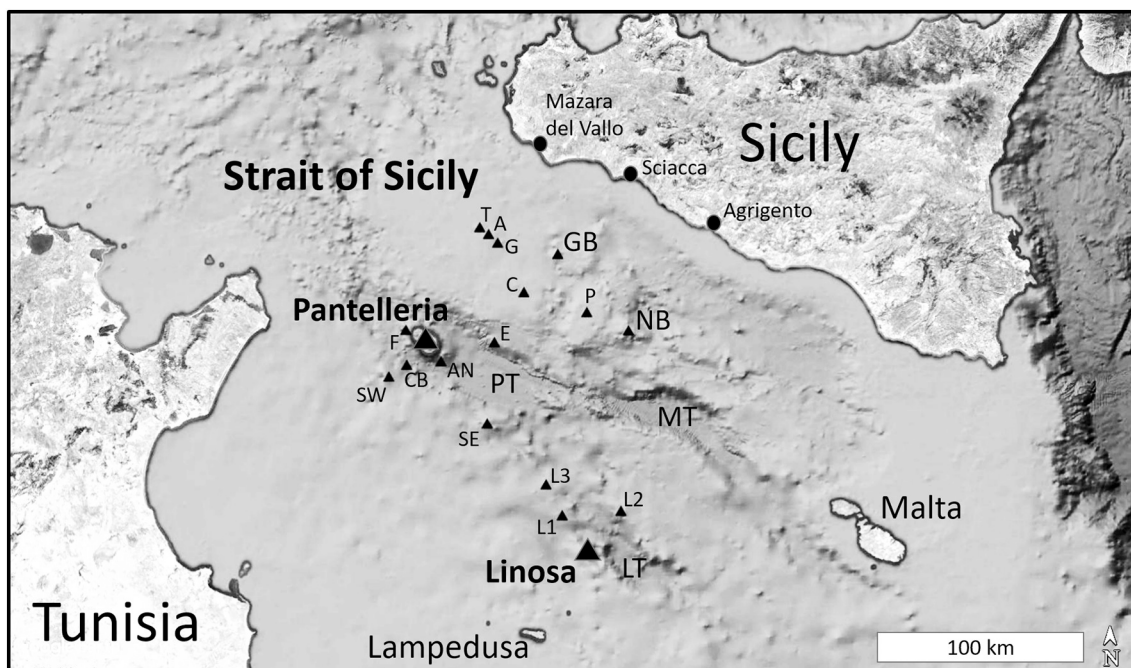
Fig. 1. Location of the Strait of Sicily, Italy-Tunisia. Rift valleys: PT, Pantelleria Trough; LT, Linosa Trough; MT, Malta Trough. Volcanic seamounts (Aissi et al., 2015): A, Anfitrite; AN, Angelina; C, Cimotoe; CB, Pantelleria Central Bank; E, Pantelleria East; F, Foerstner; GB, Graham Bank; G, Galatea; L1, Linosa I; L2, Linosa II; L3, Linosa III; NB, Nameless Bank; P, Pinne; SE, Pantelleria Southeast; SW, Pantelleria Southwest. Google Earth v.7.3.2.5776 (13 December 2015). 36.7649°N 12.8443°E, Eye alt 520 km. SIO, NOAA, US Navy, GEBCO. http://www.earth.google.com [20 November 2019].

Table 1
Major and trace element compositions of volcanic rocks from Pantelleria and Linosa.

Island	Pantelleria										
Sample ID	130912	130911	060532	030512	060531	030508	130916	060533	060534	130914	130913
Phase	PP	PP	NP	NP	NP	NP	PP	NP	NP	PP	PP
Lat (N)	36.8353	36.8107	36.8311	36.8366	36.8269	36.8197	36.8261	36.8389	36.8361	36.8217	36.8214
Long (E)	11.9691	11.9286	11.9367	11.9477	11.9556	11.9286	11.9364	11.9519	11.9678	11.9519	11.9287
Class	tB	aB	aB	tB	aB	AB	aB	aB	aB	aB	HAW
SiO_2, wt%	50.36	47.14	47.72	47.83	48.23	46.52	48.69	47.93	46.31	48.59	50.90
TiO_2	2.05	2.89	2.63	2.65	2.63	3.13	2.88	2.94	3.15	2.81	2.14
Al_2O_3	13.13	14.85	15.42	15.47	15.82	14.22	15.05	15.02	14.71	15.63	15.65
$Fe_2O_3^T$	10.50	13.22	11.72	12.14	11.94	13.63	12.98	12.66	12.89	12.79	10.62
MnO	0.17	0.19	0.17	0.16	0.16	0.18	0.19	0.18	0.18	0.18	0.18
MgO	7.43	7.08	6.44	6.27	6.23	6.12	5.87	5.82	5.79	5.78	5.66
CaO	9.69	10.65	11.17	11.08	11.33	10.48	10.69	10.56	10.57	10.89	9.42
Na_2O	2.98	3.28	3.21	2.92	3.09	3.16	3.35	3.52	3.33	3.27	3.61
K_2O	1.26	0.93	1.03	0.76	0.89	0.90	1.00	1.04	0.98	0.98	1.50
P_2O_5	0.64	0.76	0.67	0.48	0.52	0.61	0.65	0.72	0.91	0.64	0.46
LOI	0.24	−0.36	0.00	0.00	0.00	0.00	−0.67	0.00	0.00	−0.60	0.20
Total	98.45	100.63	100.19	99.77	100.84	98.95	100.68	100.40	98.82	100.96	100.34
Mg#	60.89	54.09	54.73	53.19	53.44	49.69	49.87	50.28	49.70	49.86	53.97
Sc, ppm	22	31	30	32	31	33	32	30	30	31	25
V	176	307	274	280	295	323	320	312	320	313	226
Cr	270	90	130	101	120	91	100	100	70	100	100
Co	37	43	36	64	39	58	38	29	35	38	32
Ni	170	80	65	57	60	57	50	41	43	150	70
Cu	20	40	53	n.a.	78	n.a.	40	33	44	40	50
Zn	130	90	75	94	76	103	100	80	82	100	110
Ga	22	19	19	17	20	17	21	16	19	21	22
Ge	1.8	1.7	1.1	1.6	1.1	1.6	2	0.9	1.2	1.6	1.7
Rb	39	14	18	12	14	13	16	13	17	15	25
Sr	523	492	530	485	492	421	472	491	499	481	418
Y	45.0	21.4	25.6	22.1	23.9	25.3	24.4	22.2	28.9	23.9	32
Zr	454	126	137	128	136	139	147	153	140	145	239
Nb	106.0	33.2	41.6	53.5	32.3	36.1	39.4	36.2	39.1	37.6	59.8
Ba	288	373	465	219	233	304	335	348	426	338	409
La	71.80	24.3	32.9	26.0	25.5	28.80	25.6	28.9	34	25.2	38.3
Ce	136.00	51.3	64.3	49.6	51.3	56.77	54.5	59.6	70.4	53.1	72.6
Pr	15.80	6.67	8.24	6.12	6.56	6.98	6.97	7.37	9.15	6.74	9.24
Nd	59.20	29.5	32.9	27.4	25.8	31.04	30.4	28.4	36.2	29.6	37
Sm	11.90	6.17	7.7	6.35	6.37	7.37	6.76	6.92	8.64	6.63	7.45
Eu	2.75	2.65	3.02	2.30	2.37	2.74	2.65	2.59	3.58	2.44	2.53
Gd	10.80	6.54	6.87	6.39	5.89	7.32	6.59	5.95	7.93	6.35	7.5
Tb	1.72	0.94	1.08	1.02	0.92	1.12	1.01	0.97	1.19	0.96	1.18
Dy	9.46	5.17	5.61	5.24	5.07	5.91	5.38	5.4	6.1	5.16	6.59
Ho	1.75	0.92	0.94	0.95	0.87	1.07	0.95	0.94	1.05	0.95	1.24

(continued on next page)

3

Table 1 (*continued*)

Island	Pantelleria								Linosa	
Er	4.96	2.38	2.5	2.28	2.82	2.52	2.5	2.79	2.54	3.24
Tm	0.73	0.308	0.342	0.316	0.38	0.323	0.346	0.361	0.317	0.482
Yb	4.49	1.80	2.12	1.97	2.19	1.9	2.11	2.22	2	2.9
Lu	0.64	0.262	0.3	0.288	0.33	0.298	0.294	0.319	0.294	0.393
Hf	10.80	3.2	4	3.8	4.29	3.7	4	4	3.5	5.5
Ta	5.96	2.11	2.75	2.1	3.17	2.18	2.51	2.59	2.28	3.43
Th	10.10	2.59	2.62	2.16	2.20	2.58	2.38	2.37	2.72	4.71
U	2.88	0.55	3.13	2.26	0.63	0.72	2.37	1.8	0.64	1.36

Island	Pantelleria	Linosa								
Sample ID	130915	130934	130933	130936	130937	130935	130939	130938	130941	130932
Phase	PP	MB	MB	AB	AB	AB	MB	MB	AB	MB
Lat (N)	36.8260	35.8745	35.8728	36.8261	35.8629	35.8635	35.8624	35.8568	35.8580	35.8549
Long (E)	11.9799	12.8709	12.8790	11.9364	12.8545	12.8586	12.8620	12.8717	12.8676	12.8805
Class	aB	aB	aB	tB	HAW	HAW	tB	HAW	HAW	HAW
SiO_2, wt%	46.22	46.37	45.71	49.62	49.43	49.56	48.87	49.22	49.63	50.80
TiO_2	3.97	2.21	2.16	2.19	2.24	2.19	2.24	2.32	2.28	2.27
Al_2O_3	13.83	14.03	13.81	15.97	16.05	15.76	16.85	16.39	16.66	16.46
$Fe_2O_3^T$	15.58	11.68	11.87	11.50	11.46	11.36	11.04	11.26	11.19	11.14
MnO	0.22	0.18	0.18	0.17	0.17	0.17	0.14	0.18	0.18	0.18
MgO	5.15	11.40	11.39	5.93	5.84	5.63	5.20	5.10	5.10	4.79
CaO	10.27	9.90	9.41	8.98	8.95	8.83	10.50	8.91	8.74	8.66
Na_2O	3.41	3.20	2.97	3.73	3.87	3.86	3.22	4.04	4.22	4.39
K_2O	1.03	1.32	1.30	1.20	1.22	1.26	0.98	1.52	1.59	1.71
P_2O_5	1.35	0.52	0.57	0.48	0.47	0.46	0.40	0.62	0.62	0.61
LOI	−0.88	0.11	−0.14	−0.34	0.03	−0.49	0.87	0.03	−0.46	−0.31
Total	100.15	100.92	99.23	99.44	99.73	98.59	100.32	99.59	99.75	100.70
Mg#	42.11	68.23	67.86	53.15	52.86	52.16	50.89	49.91	50.07	48.61
Sc, ppm	30	26	26	23	22	22	29	23	22	22
V	374	233	228	206	202	204	236	204	199	205
Cr	30	450	490	180	160	160	290	120	100	100
Co	38	50	53	35	34	33	32	31	28	29
Ni	40	250	270	80	80	70	70	60	60	50
Cu	20	50	60	60	60	40	60	30	40	40
Zn	180	80	90	110	100	100	170	100	100	110
Ga	22	18	18	21	21	21	20	22	22	23
Ge	1.7	1.6	1.5	1.6	1.8	1.7	2.3	1.7	1.6	1.7
Rb	15	25	26	22	22	22	16	27	29	30
Sr	515	537	523	411	427	422	446	467	488	460
Y	31.2	20.1	21.3	24.5	24.1	24.4	22	28.9	28.9	30.3
Zr	158	194	189	186	187	189	139	237	239	259
Nb	42.2	46.4	49.2	40.6	41.3	40.5	28.3	52	52.4	56.2
Ba	378	342	344	257	261	267	184	321	330	344
La	34.1	29.6	29.4	24.5	22.7	23.9	16.5	31.2	30.4	33.5
Ce	73.5	60.1	58.9	51.1	46.8	49.5	35.5	63	62.9	67.4
Pr	9.98	7.17	7.29	6.24	5.91	6.17	4.59	7.77	7.55	8.28
Nd	44	28.9	28.9	25.6	24.4	25.8	19.8	31.8	32.1	33.7
Sm	9.4	5.71	5.79	5.78	5.49	5.82	4.96	7.07	6.94	7.02
Eu	3.66	2	1.92	1.93	1.9	2.01	1.74	2.34	2.29	2.31
Gd	9.66	5.65	5.56	5.83	5.76	6.04	5.02	6.75	6.75	6.9
Tb	1.41	0.84	0.82	0.96	0.88	0.96	0.79	1.05	1.04	1.1
Dy	7.22	4.57	4.49	5.06	5.01	5.19	4.51	5.99	5.77	6.39
Ho	1.28	0.84	0.79	0.94	0.92	0.95	0.82	1.12	1.09	1.18

4

Table 1 (continued)

Island	Pantelleria	Linosa									
Er	3.21	2.29	2.18	2.4	2.63	2.52	2.61	2.32	3.14	3.11	3.43
Tm	0.438	0.34	0.317	0.339	0.394	0.369	0.377	0.323	0.461	0.432	0.494
Yb	2.52	1.99	1.87	2.14	2.33	2.3	2.35	1.91	2.8	2.89	3.04
Lu	0.345	0.295	0.276	0.3	0.312	0.326	0.316	0.272	0.422	0.422	0.439
Hf	3.9	4.6	4.4	4.5	4.4	4.3	4.5	3.2	5.2	5.1	5.6
Ta	2.64	2.73	2.72	3.29	2.55	2.28	2.36	1.73	3.03	2.89	3.27
Th	3.01	3.99	3.74	4.06	2.88	2.74	2.85	1.74	4.27	4.12	4.16
U	0.53	1.51	1.14	1.25	0.82	0.87	0.88	0.56	1.09	1.16	1.2

Phases of mafic volcanism for Pantelleria (following Civetta et al., 1998; Avanzinelli et al., 2004); PP, paleo-Pantelleria (120 and 80 ka); NP, neo-Pantelleria (29 and 10 ka). Phases of mafic volcanism for Linosa (following Lanzafame et al., 1994): AB, Arena Bianca (700 ka); MB, Monte Bandiera (530 ka).

Class (Le Maitre, 2002): aB, alkali basalt; tB, transitional basalt; HAW, hawaiite. $Fe_2O_3^T$, total iron reported as Fe_2O_3; LOI, loss on ignition; Mg# = mol Mg/(Mg + Fe^{2+}), assuming Fe^{2+} = $0.9Fe^T$; n.a., not analyzed.

geothermobarometry to determine the average depth of partial melting and temperature of melt segregation from calculated primary basalts (Lee et al., 2009); (2) the use of major- and trace-element ratios to constrain mantle sources (e.g., Jackson and Dasgupta, 2008; Stracke and Bourdon, 2009; Dasgupta et al., 2010; Davis et al., 2013; Yang and Zhou, 2013); and (3) rare earth element (REE) inverse models using the INVMEL algorithm to constrain mantle source composition and the degree and depth range of partial melting (McKenzie and O'Nions, 1991, 1995). The second goal of this paper is to use the results of these various geochemical models to: (1) determine the conditions of partial melting in the asthenosphere beneath the SSRZ; (2) discriminate between the effects of lithospheric thickness, source lithology, and magma storage on the geochemistry of these basalts; and (3) constrain the magma storage conditions in the crust and describe its effect on basalt geochemistry.

2. Geologic setting

The SSRZ is a northwest-southeast trending transtensional rift system situated on the Pelagian Block, the northern promontory of the African plate that represents the foreland domain of the Apennine-Sicilian-Maghrebian orogen (Catalano et al., 2009; Martinelli et al., 2019). The SSRZ consists of three basins: the Pantelleria Trough, the Linosa Trough, and the Malta Trough. Water depth is < 400 m beneath most of the Pelagian Block, increasing to ~1350 m in the Pantelleria Trough, ~1580 m in the Linosa Trough, and ~1720 m in the Malta Trough (Calanchi et al., 1989; Civile et al., 2010). Volcanoes are present in or adjacent to all except the Malta Trough, and include two islands (Pantelleria and Linosa) and several seamounts. The thickness of the crust throughout most of the Pelagian Block is 25–35 km, thinning to 16–18 km beneath the troughs, 20–21 km beneath the island of Pantelleria, and 24–25 km beneath the island of Linosa (Civile et al., 2008; Catalano et al., 2009). The depth to the lithosphere-asthenosphere boundary has been inferred from regional geophysical studies. The Pelagian Block is characterized by high heat flow (> 80 mW/m^2) with values that increase to > 130 mW/m^2 in the Pantelleria and Linosa troughs (Della Vedova et al., 1995) and up to 200–460 mW/m^2 within the Cinque Denti caldera (Bellani et al., 1995). Combined with positive Bouguer anomalies (65–103 mgal; Berrino and Capuano, 1995), several workers have suggested asthenospheric upwelling up to ~60 km (Della Vedova et al., 1995; Argnani and Torelli, 2001; Civile et al., 2008).

Extension of the SSRZ began ~7 Ma, with minor volcanism occurring during the late Miocene (Messinian) and the vast majority of volcanism occurring during the Plio-Pleistocene (Calanchi et al., 1989; Rotolo et al., 2006; Coltelli et al., 2016; Lodolo et al., 2019; Martinelli et al., 2019). Volcanic seamounts are primarily located in one of three areas within the SSRZ (Fig. 1; Aissi et al., 2015): (1) the Graham and Terrible volcanic province (Anfirite, Tetide, Galatea, Graham Bank, Cimotoe, Pinne, and Nameless Bank volcanoes), which lies 50–75 km offshore and runs parallel to the coast of Sicily for ~100 km between Mazara del Vallo and Agrigento (Lodolo et al., 2019); (2) near the island of Pantelleria (Pantelleria SE, Pantelleria E, Pantelleria SW, Pantelleria Central Bank, Angelia, and Foerstner volcanoes); and (3) north of the island of Linosa (Linosa I, Linosa II, and Linosa III volcanoes). Within the Graham and Terrible volcanic province, the oldest (late Miocene) is the Nameless Bank seamount, which lies ~100 km east of Pantelleria and ~70 km southwest of Agrigento and rises from a depth of 330–340 m to 80–90 m b.s.l.; the youngest is the Graham Bank seamount, which is located ~50 km southwest of Sciacca and ~70 km northwest of Pantelleria, rises from 330–340 m to 7 m b.s.l., and last erupted in 1831 CE (producing the ephemeral "Ferdinandea Island"; Gemmellaro, 1831; Washington, 1909; Kelly et al., 2014; Cavallaro and Coltelli, 2019.)

The island of Pantelleria is by far the larger (83 km^2 surface area; 580 km^2 total) of the two islands and represents the emergent portion of a volcanic edifice that rises 836 m above sea level and ~2200 m above

the sea floor within the Pantelleria graben (Calanchi et al., 1989; Civile et al., 2010). Most rocks exposed on the island are felsic, volcanic (trachyte-pantellerite), and younger than the 45.7 ± 1.0 ka pantelleritic Green Tuff, the caldera-forming ignimbrite of the Cinque Denti caldera (Mahood and Hildreth, 1986; Scaillet et al., 2013). The oldest exposed pantelleritic lava on the island has been dated at 324 ± 11 ka (Mahood and Hildreth, 1986), but most of the island is submerged, much older, and most likely primarily basaltic (Fulignati et al., 1997). The oldest documented basalts (~80–120 ka, herein termed "paleo-Pantelleria", following Avanzinelli et al., 2004) are exposed primarily in outcrops along the coast and along the scarp of the Cinque Denti caldera (Mahood and Hildreth, 1986). Younger mafic lavas ("neo-Pantelleria") are found in the northwestern part of the island and include flows that erupted at ~29 ka from the Cuddia Bruciata, Cuddia Ferle, and Cuddia del Monte cinder cones, and at ~10 ka from the Cuddie Rosse cinder cone (Mahood and Hildreth, 1986; Civetta et al., 1998). The most recent volcanic activity occurred ~4 km NW of the island at the submarine (250 m b.s.l.) Foerstner volcano on 17–25 October 1891 CE (Washington, 1909; Conte et al., 2014; Kelly et al., 2014).

The island of Linosa lies ~120 km to the southeast of Pantelleria. Linosa is much smaller (5.4 km² surface area; 159 km² total) and represents the emergent portion of a large submarine volcanic complex that rises 196 m above sea level and ~800 m above the sea floor along the SW edge of the Linosa graben (Rossi et al., 1996; Tonielli et al., 2019; Romagnoli et al., 2020). Linosa is dominated by mafic lavas and tuffs that erupted in three stages at 1070 ka (paleo-Linosa), 700 ka (Arena Bianca), and 530 ka (Monte Bandiera) and created several coalescing cinder cone and maar volcanoes (Lanzafame et al., 1994). The paleo-Linosa stage is characterized primarily by hydromagmatic pyroclastic sequences with minor scoria and lava which built maars and cinder cones. The beginning of the Arena Bianca stage was dominated by hydromagmatism followed by eruptions of scoria that built the Monte Nero cinder cone and lava flows that created the eastern third of the present-day island. The Monte Bandiera stage also began with hydromagmatic activity that created the Fossa Cappellano maar volcano (and associated Monte Bandiera tuff ring), which was followed by eruptions of scoria and lava that built the Montagna Rossa and Monte Vulcano cinder cones that dominate the western two-thirds of the island (Rossi et al., 1996).

3. Methods and results

3.1. Methods and materials

Twenty-two samples of mafic lava and scoria were collected from the islands of Pantelleria (12) and Linosa (10) during field trips in 2003, 2006 and 2013, six of which were originally presented in Parker and White (2008) and White et al. (2009). These samples were powdered to −200 mesh in a pre-contaminated shatterbox grinder and were analyzed at Activation Laboratories, Ontario, for major-elements by ICP-OES and trace-elements (including a full suite of rare earth elements [REE]) by ICP-MS (Code 4Lithoresearch). Whole-rock analyses are presented in Table 1. For the discussion that follows, these analyses are combined with data from literature for a total of 134 analyses of mafic rocks (SiO_2 ≤ 52 wt% normalized anhydrous); 75 of these include analyses of REE, including 39 from Pantelleria (Civetta et al., 1998; Esperança and Crisci, 1995; Avanzinelli et al., 2004, 2014), 29 from Linosa (Bindi et al., 2002; Di Bella et al., 2008; Avanzinelli et al., 2014), and 7 from various Seamounts (Rotolo et al., 2006; with additional data from Beccaluva et al., 1981, and Calanchi et al., 1989). Excluded are the Khartibucale hawaiites at Pantelleria, which deserve a separate study; they have trace-element and isotopic signatures significantly different from the rest of the SSRZ mafic lavas and there are only three known published analyses, each of which is too evolved (MgO < 5 wt %, Ni < 10 ppm) to be reliably used with the models presented in this
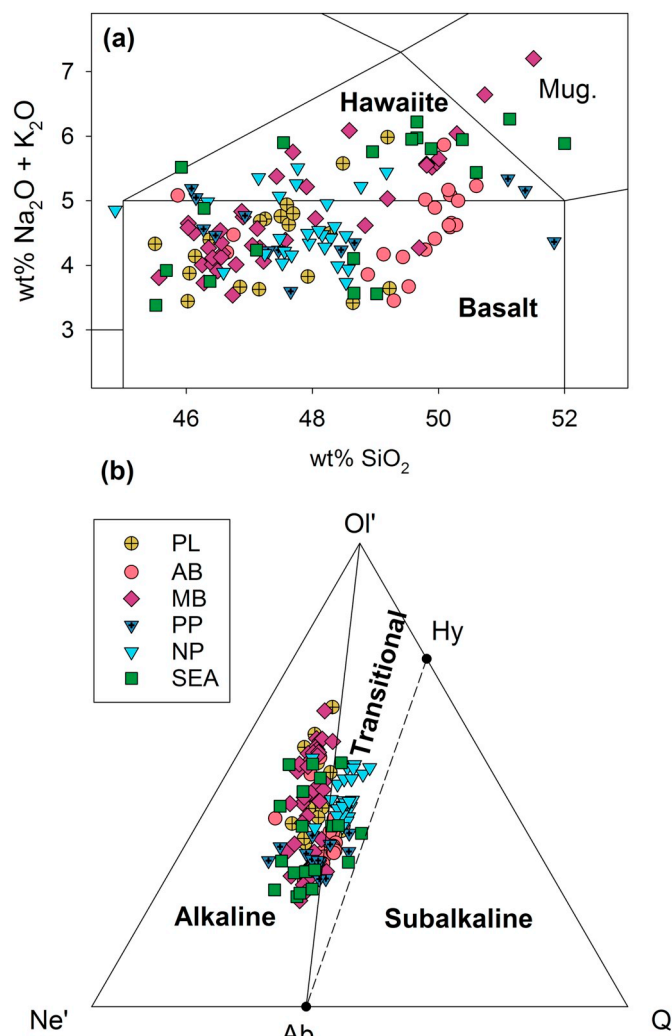

Fig. 2. (a) Total-alkali versus silica (TAS) diagram for the classification of volcanic rocks (Le Maitre, 2002). (b) Basalt tetrahedron projected from clinopyroxene: Q' = q + 0.4ab + 0.25hy; Ol' = ol + 0.75hy; Ne' = ne + 0.6ab (Irvine and Baragar, 1971). Alkali basalts plot below the plane of critical silica undersaturation (solid line); transitional basalts plot below the plane of critical silica saturation (dashed line). Units: PL, Paleo-Linosa; AB, Arena Bianca (Linosa); MB, Monte Bandiera (Linosa); PP, Paleo-Pantelleria; NP, Neo-Pantelleria; SEA, Seamounts.

study (Avanzinelli et al., 2004, 2014; White et al., 2009).

3.2. Major-element geochemistry

All but five samples classify as either basalt or hawaiite (Fig. 2a; Le Maitre, 2002), with basalts further classified based on normative mineralogy (assuming FeO/FeO* = 0.9) as either alkali basalt (ol + ne-normative) or transitional basalt (ol + hy-normative) on their position in the basalt tetrahedron (Fig. 2b; Irvine and Baragar, 1971). Linosa samples from the 1070 ka paleo-Linosa and 530 ka Monte Bandiera stages are dominated by alkali basalt, with the samples evolving from Ol' (=normative ol + 0.25hy) towards normative Ab along the Ol'-Ab join, which divides the "alkali" and "transitional" basalt fields. Linosa samples from the 700 ka Arena Bianca stage along with most Pantelleria samples classify predominantly as transitional basalts. Mafic lavas and scoriae from both trends are petrographically broadly similar, consisting of porphyritic rocks with variable amounts of phenocrysts of olivine, clinopyroxene, plagioclase, and magnetite (Rossi et al., 1996; Civetta et al., 1998; Bindi et al., 2002; Di Bella et al., 2008; and White
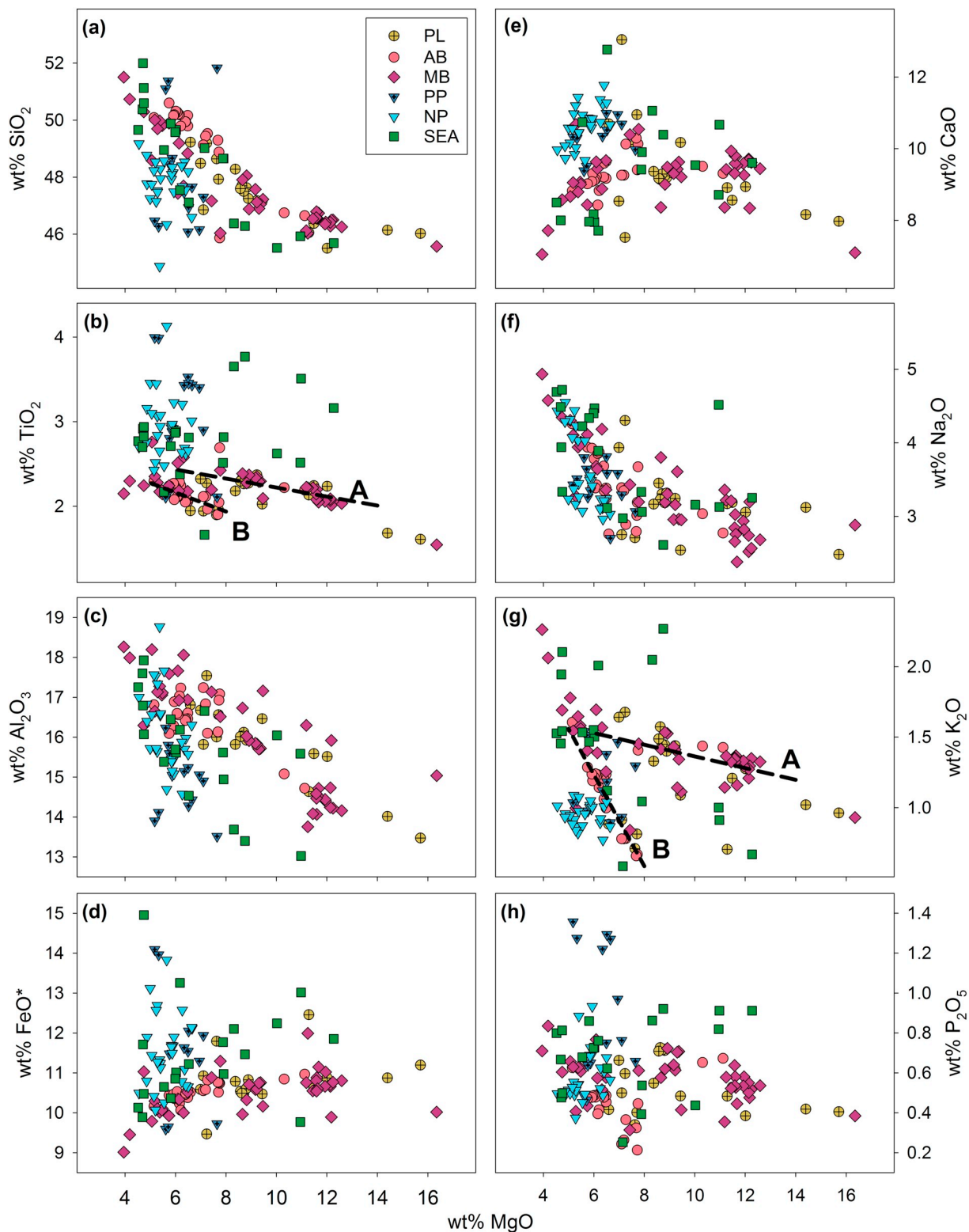
Fig. 3. Major-element variation diagrams that use MgO as the differentiation index. Dashed lines illustrate the two major trends (see text for details.) Units: PL, Paleo-Linosa; AB, Arena Bianca (Linosa); MB, Monte Bandiera (Linosa); PP, Paleo-Pantelleria; NP, Neo-Pantelleria; SEA, seamounts. Trends labelled A and B correspond to the Linosa trends of Di Bella et al. (2008).

et al., 2009 provide comprehensive descriptions).

Major-element variation diagrams that use wt% MgO as a differentiation index are plotted in Fig. 3. Several differences can be seen between and within the Pantelleria and Linosa suites. Primitive basalts (MgO > 9 wt%) have not been documented at Pantelleria (max

7.65 wt%, median 5.82 wt% MgO), but have been at Linosa (max 16.35 wt%, median 7.72 wt% MgO). However, basalts with very high (> 14 wt%) MgO at Linosa likely resulted from the accumulation of olivine (Di Bella et al., 2008). At a given concentration of MgO, Linosa basalts have higher SiO₂ and Al₂O₃, but lower FeO*, TiO₂, and CaO
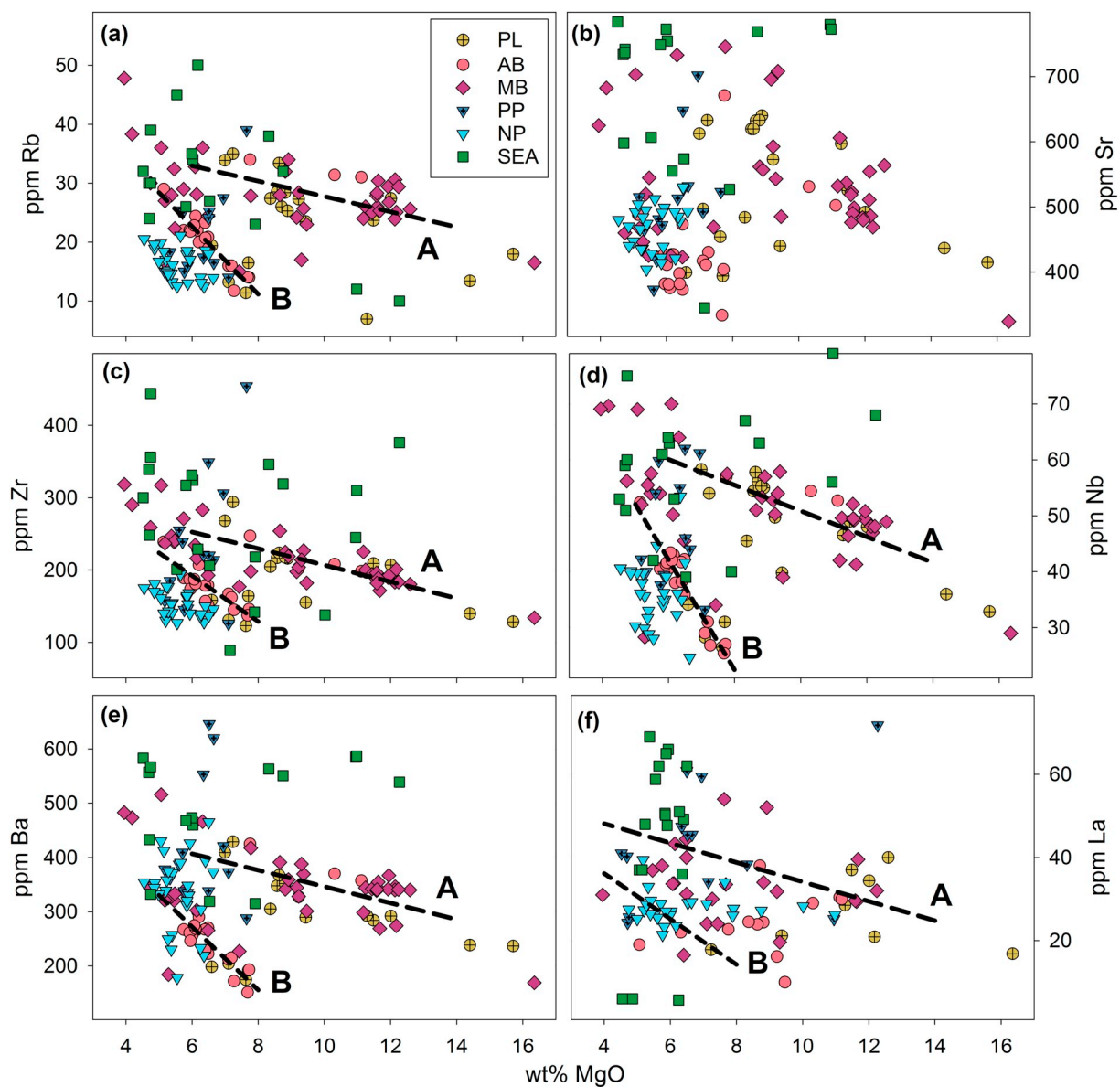
Fig. 4. Trace-element variation diagrams that use MgO as the differentiation index. Units: PL, Paleo-Linosa; AB, Arena Bianca (Linosa); MB, Monte Bandiera (Linosa); PP, Paleo-Pantelleria; NP, Neo-Pantelleria; SEA, seamounts. Trends labelled A and B correspond to the Linosa trends of Di Bella et al. (2008).

than Pantelleria basalts (Fig. 3a, b, c, d, e). Within the Linosa samples, CaO increases with decreasing to MgO to ~8 wt% after which it de-creases. Two distinct trends are observed in plots of TiO_2 and K_2O versus MgO (Fig. 3b, g). The higher-TiO_2, K_2O, and P_2O_5 trend (labelled "A", following Di Bella et al., 2008) includes most of the younger Monte Bandiera (MB) basalts from Linosa and some samples from the older suites; The lower-TiO_2, K_2O, and P_2O_5 trend (labelled "B", following Di Bella et al., 2008) includes most of the older Arena Bianca (AB) basalts from Linosa and some samples from both MB and the older Paleo-Linosa (PL) suites. The younger basalts from Pantelleria (neo-Pantelleria; NP) form trends similar to Trend B with respect to K_2O (but at slightly lower values) and P_2O_5 but with considerably higher TiO_2, whereas the older basalts (paleo-Pantelleria; PP) define no coherent trend, and are char-acterized by even higher TiO_2 (> 3 wt%) and P_2O_5 (> 1 wt%) than the NP basalts (Civetta et al., 1998). Bindi et al. (2002) and Di Bella et al. (2008) attributed the origin of the two suites at Linosa as the result of fractional crystallization from similar, hypothetical parental basalts at different pressures, with "Trend-A" representing a younger suite that crystallized at higher pressures based on clinopyroxene crystal chem-istry. In contrast, Civetta et al. (1998) attributed the differences

between the High Ti-P and Low Ti-P suites of Pantelleria to variable degrees of partial melting from a heterogeneous mantle source in ad-dition to fractional crystallization.

3.3. Trace-element geochemistry

Trace-element variation diagrams that use MgO as a differentiation index are plotted in Fig. 4. As with the major-element geochemistry, trace-element concentrations and ratios show great diversity both be-tween and within the island suites. Ni, Cr and Co (not shown), de-monstrate a constant and linear decrease with MgO indicating fractio-nation (or accumulation in the case of high-MgO samples) of olivine throughout the suite. Unlike the transition elements, the large-ion li-thophile elements (LILE: Rb, Sr, Ba, and La) and high field-strength elements (HFSE: Zr, Nb) form distinct trends, similar to K_2O and TiO_2. Trend-A is again dominated by the Monte Bandiera (MB) lavas from Linosa, and includes a few samples from the other Linosan suites as well as some of the paleo-Pantelleria (PP) samples, whereas Trend-B consists of the Arena Bianca (AB) lavas from Linosa as well as a few samples from the other Linosan suites as well as most of the neo-Pantelleria (NP)
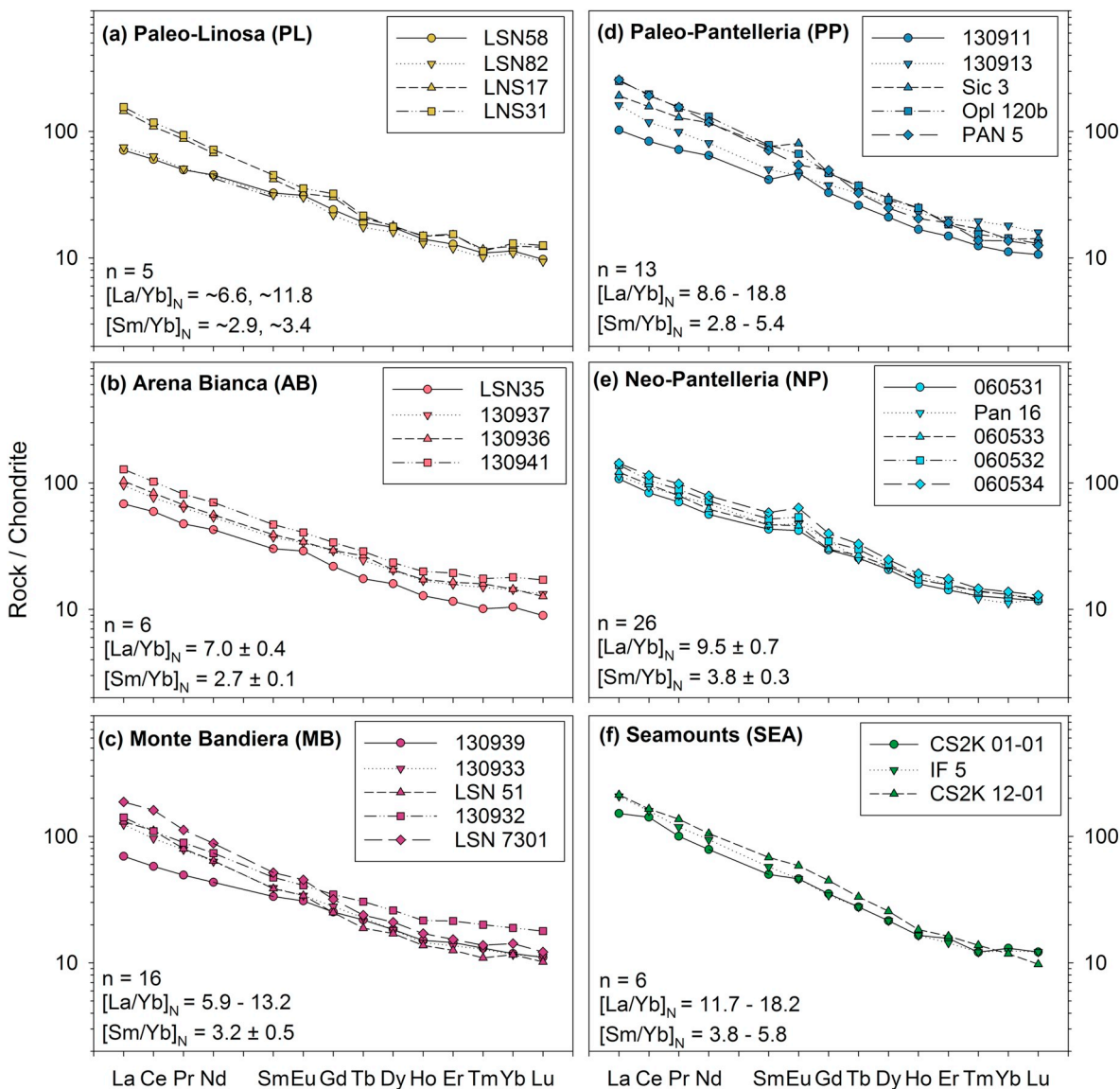
Fig. 5. Representative rare-earth element diagrams (normalized to CI Chondrite; McDonough and Sun, 1995). In each graph, n = the total number of analyses in the dataset. REE ratios are reported either as a range or averages with standard deviation.

samples and some of the PP samples. At a given value of MgO, the NP samples demonstrate slightly lower values of Rb, Zr, Nb, and La than the MB samples.

Representative rare earth element (REE) diagrams (normalized to CI chondrite; McDonough and Sun, 1995) are presented in Fig. 5. Arena Bianca (AB; Fig. 5b) and neo-Panelleria (NP; Fig. 5e) display the most constant values, with La_N/Yb_N enrichments of ~7.0 and 9.5 and Sm_N/Yb_N enrichments of ~2.7 and 3.8, respectively. Monte Bandiera (MB; Fig. 5c) has a large range of La_N/Yb_N values, but near-constant Sm_N/Yb_N. Paleo-Linosa samples (PL; Fig. 5a) have similar HREE concentrations, but La_N/Yb_N values either more similar to AB or MB. Paleo-Pantelleria (PP) and the seamounts (SEA) have the least internal consistency, at least in part because unlike the others they represent discrete volcanic centers that erupted over ~120 ka and 8 Ma, respectively. Several PP samples have La_N/Yb_N and Sm_N/Yb_N ratios similar to NP. Positive Eu anomalies (i.e., $Eu_N/Eu^* > 1.0$, with $Eu^* = [Sm_N \cdot Gd_N]^{1/2}$) characterize basalts on both islands, with Pantelleria basalts (PP $Eu_N/Eu^* = 1.13 \pm 0.17$; NP $Eu_N/Eu^* = 1.17 \pm 0.09$) having a more pronounced anomaly than Linosa basalts ($Eu_N/Eu^* = 1.06 \pm 0.07$). Positive Eu anomalies are a common feature in primitive (MgO > 9 wt%) MORB and OIB and have been interpreted

as evidence of mixing of DMM with recycled lower continental lithosphere (Niu and O'Hara, 2009; Tang et al., 2015); however, the lack of a negative correlation between Eu_N/Eu^* and radiogenetic lead isotope ratios makes lower continental crust an unlikely component. Likewise, the ubiquity of the positive Eu anomaly in SSRZ basalts coupled with its presence in aphyric and low-phyric basalts, along with a lack of correlation between Eu_N/Eu^* and Sr, strongly suggests that plagioclase accumulation is an unlikely mechanism for producing this anomaly in these rocks (Civetta et al., 1998; Bindi et al., 2002; Di Bella et al., 2008; White et al., 2009). Alternatively, a positive Eu anomaly may simply be due the relative incompatibility of divalent Eu in clinopyroxene compared to trivalent Gd and Sm, coupled with more reducing conditions in the source region which leads to higher Eu^{2+}/Eu^{3+} and thus higher Eu_N/Eu^* in the partial melts (Tang et al., 2017).

4. Discussion

4.1. Fractional crystallization and magma storage

Models of fractional crystallization/accumulation processes and magma storage conditions are evaluated using Pearce (1968) element
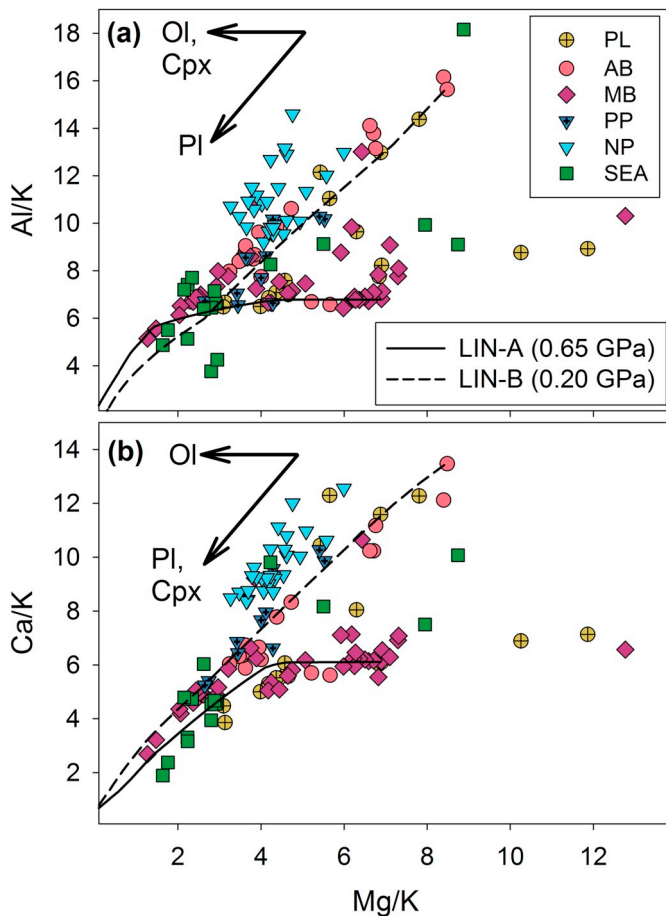
Fig. 6. Pearce (1968) element ratios plotted with the results of MELTS (rhyolite-MELTS v.1.0.2; Gualda et al., 2012) models of fractional crystallization at 0.20 and 0.65 GPa. Vectors show the slopes of the data distribution trends that would result from the fractionation of olivine (Ol), clinopyroxene (Cpx), and plagioclase (Pl).

ratio (PER) diagrams coupled with the results of thermodynamic (MELTS) modelling. PER diagrams plot ratios of major elements or combinations of major elements with a common incompatible, or "conserved", element (e.g., Mg/K vs. Ca/K or [Si + Al]/Zr vs. [Na + K]/Zr). Interpretations of these diagrams are based on the stoichiometry of rock-forming minerals, and slopes of data distributions are equal to major element ratios of minerals lost or gained during differentiation of a cogenetic suite of rocks (Russell and Nicholls, 1988). For example, data plotted with Mg/K on the abscissa and Ca/K or Al/K on the ordinate will form a linear trend with a slope that varies depending on the fractionating or accumulating assemblage from horizontal for a phase with non-stoichiometric Ca or Al (e.g., olivine) to vertical for a phase with non-stoichiometric Mg (e.g., plagioclase). Diagrams plotting Mg/K versus Al/K (Fig. 6a) and Ca/K (Fig. 6b) can therefore be used to discriminate between fractionation or accumulation of olivine (horizontal slopes on both diagrams with decreasing Mg/K), clinopyroxene (horizontal slope with Al/K and a positive slope with Ca/K versus Mg/K), and plagioclase (positive slopes on both diagrams). The two Linosa trends (hereafter LIN-A and LIN-B) observed in the major- and trace-element variation diagrams (Figs. 3 and 4) are also seen in the PER diagrams. These first preclude the possibility of a common parental magma for the two trends; linking LIN-A and LIN-B by fractional crystallization would require the crystallization of geologically implausible mineral assemblages. PER diagrams suggest that LIN-A is formed by a paragenetic sequence of olivine to olivine + clinopyroxene to clinopyroxene + plagioclase ± olivine and LIN-B is

formed by a continuous sequence of plagioclase + clinopyroxene ± olivine. Samples with Mg/K > 12 correspond to those with MgO > 14 wt% and are most likely the result of olivine accumulation. Both trends converge at Mg/K ≈ 4, which corresponds to MgO ≈ 6.5 wt%. Pantelleria basalts form a trend subparallel to LIN-B, suggesting that these magmas evolved along a similar liquid line of descent.

These interpretations are in accord with the results of thermodynamic models of fractional crystallization. Models were produced using the MELTS algorithm (rhyolite-MELTS v. 1.0.2; Ghiorso and Sack, 1995; Asimow and Ghiorso, 1998; Gualda et al., 2012), the results of which are superimposed on the data in Fig. 6. The models presented were calculated under anhydrous conditions with oxygen fugacities fixed to the fayalite-magnetite-quartz (FMQ) buffer and a step size of 5 °C. LIN-A is most successfully modelled as fractional crystallization from the most primitive MB basalt (LSN51, 12.59 wt% MgO, Mg# = 0.70, 278 ppm Ni; Di Bella et al., 2008) at 0.65 GPa. At this pressure olivine is the liquidus phase at 1376 °C, and is replaced by clinopyroxene at 1281 °C (MgO^{liq} = 8.83 wt%, F = 0.89), which is joined by plagioclase at 1191 °C (MgO^{liq} = 4.40 wt%, F = 0.56). In contrast, LIN-B is best modelled as the result of fractional crystallization from the most primitive AB basalt (LNS40, 7.68 wt% MgO, Mg# = 0.59, 85 ppm Ni; Bindi et al., 2002) at 0.2. At this pressure, olivine is the liquidus phase at 1206 °C, and is closely joined by plagioclase at 1201 °C (MgO^{liq} = 7.45 wt%, F = 0.95), and clinopyroxene at 1196 °C (MgO^{liq} = 7.26 wt%, F = 0.89). These models are consistent with the mass balance models discussed by Di Bella et al. (2008) and the conclusions of Bindi et al. (2002), who used evidence from clinopyroxene crystal chemistry to suggest that the depth and pressure of fractional crystallization at Linosa increased with time from 700 ka (AB) to 530 ka (MB). Assuming average crustal density of 2700 km, this places the magma reservoir at ~7.6 km for the largely older LIN-B suite and ~24.6 km for the younger LIN-A suite; these values correspond closely to the depths of the top of the crystalline basement (~8 km) and the Moho (24–25 km) beneath Linosa, respectively (Civile et al., 2008). Thermodynamic models for the younger Pantelleria basalts (NP) reported by White et al. (2009) have results similar to LIN-B, but require lower pressures (0.10 GPa) and more hydrous conditions (1.0–1.5 wt% H$_2$O) with olivine on the liquidus at 1135 ± 10 °C, followed by clinopyroxene at 1125 ± 10 °C and plagioclase at 1085 ± 10 °C.

4.2. Primary magma compositions and constraints on pressure and temperature of melt generation

An estimate of the composition of primary basalts is necessary to determine the conditions of partial melting in the mantle, such as the temperature, pressure/depth of melt segregation, and melt fraction produced. However, every basalt has undergone some degree of fractionation and assimilation prior to eruption and even if assimilation is assumed to be negligible, once the fractionating magma is multiply saturated it becomes very difficult to back-calculate the liquid line of decent (O'Hara, 1968). To do so, of course, first requires the assumption that the rock sample is relatively unweathered and has undergone only olivine fractionation; for this reason, we include only relatively primitive samples characterized by very low (< 1 wt%) LOI, relatively high (> 10 wt%) MgO, and a lack of a negative Eu anomaly. We also exclude those with very high (> 14 wt%) MgO, which could be the result of olivine accumulation (Di Bella et al., 2008). The only samples that fit these criteria are those fall along the olivine fractionation trend for LIN-A in Fig. 6 (discussed in Section 4.1). Therefore most of the remainder of the discussion will focus on the origin of the basalts of this sub-group, with inferences made for the origin of the others by comparison.

The composition of the primary magma parental to a basaltic rock may be estimated by iteratively "correcting" it for olivine fractionation until the recalculated basalt has an Mg# that has been experimentally determined to be in equilibrium with mantle peridotite (Lee et al., 2009). Calculated (anhydrous) primary basalts in equilibrium with

Table 2

Calculated primary basalt compositions and the results of olivine-liquid geothermobarometry for anhydrous and hydrous LIN-A primitive basalts.

Sample	Source	Phase	Calculated Primary Basalt Compositions (wt%)											Total	P05/A	L09	A92	L09	L09	z (km)
			SiO₂	TiO₂	Al₂O₃	Fe₂O₃	FeO	MnO	MgO	CaO	Na₂O	K₂O	H₂O		T (°C)	P (GPa)	P (GPa)	T (°C)	P (GPa)	
Anhydrous																				
LSN 51	D08	MB	45.96	1.88	13.11	1.45	9.52	0.17	15.39	8.74	2.48	1.23	–	99.94	1456	2.64	2.41	1456	2.64	85.3
LSN 75	D08	MB	46.15	1.90	13.10	1.43	9.50	0.16	15.23	8.86	2.36	1.24	–	99.93	1452	2.54	2.33	1450	2.53	81.8
LSN 54	D08	MB	46.09	1.92	13.13	1.43	9.46	0.16	15.13	8.92	2.53	1.17	–	99.94	1449	2.55	2.33	1448	2.55	82.4
LSN 52	D08	MB	45.95	1.91	13.57	1.42	9.41	0.16	15.14	8.95	2.32	1.11	–	99.93	1449	2.52	2.37	1448	2.51	81.4
LSN 56	D08	MB	46.00	1.89	13.24	1.41	9.43	0.16	15.11	8.79	2.69	1.22	–	99.93	1447	2.61	2.34	1448	2.61	84.4
LSN 60	D08	MB	46.00	1.87	13.01	1.44	9.75	0.17	15.62	8.37	2.55	1.17	–	99.94	1463	2.69	2.44	1462	2.68	86.7
LSN 76	D08	MB	46.18	1.91	13.32	1.40	9.39	0.16	14.83	8.96	2.53	1.25	–	99.93	1440	2.47	2.25	1438	2.47	79.9
LSN 77	D08	MB	46.40	1.91	13.27	1.40	9.34	0.16	14.79	9.00	2.44	1.24	–	99.93	1439	2.40	2.19	1435	2.38	77.3
LSN 59	D08	MB	46.17	1.94	13.19	1.41	9.58	0.16	15.29	8.42	2.57	1.22	–	99.94	1453	2.58	2.33	1451	2.57	83.1
130934	Table 1	MB	46.14	2.03	12.85	1.39	9.35	0.16	14.82	9.07	2.93	1.21	–	99.94	1438	2.56	2.25	1441	2.58	83.3
130933	Table 1	MB	46.12	1.99	12.71	1.42	9.64	0.16	15.30	8.66	2.73	1.20	–	99.93	1453	2.63	2.35	1454	2.64	85.1
LNS31	B02	PL	45.99	2.05	14.22	1.40	9.41	0.19	14.86	7.81	2.91	1.10	–	99.95	1439	2.54	2.30	1438	2.54	82.1
LSN 63	D08	MB	46.17	1.83	13.15	1.44	9.86	0.15	15.67	8.52	2.13	1.04	–	99.95	1466	2.54	2.41	1460	2.52	81.4
130931	Table 1	MB	46.10	2.01	12.46	1.41	9.69	0.16	15.43	8.53	2.92	1.24	–	99.94	1456	2.72	2.37	1458	2.73	88.1
LNS20	B02	MB	45.62	2.00	14.62	1.39	9.54	0.15	15.06	7.50	3.02	1.03	–	99.96	1444	2.67	2.44	1446	2.68	86.4
LSN 45	D08	AB	46.16	1.95	13.12	1.41	9.76	0.16	15.35	8.29	2.47	1.27	–	99.95	1456	2.58	2.35	1452	2.57	83.1
LSN 49	D08	AB	46.15	1.95	13.24	1.38	9.71	0.15	15.11	8.34	2.66	1.26	–	99.95	1448	2.56	2.30	1446	2.56	82.7
		Average	46.08	1.94	13.25	1.41	9.55	0.16	15.18	8.57	2.60	1.19	–	99.94	1450	2.58	2.34	1449	2.57	83.2
		Stdev	0.16	0.06	0.51	0.02	0.16	0.01	0.27	0.43	0.24	0.08	–	0.01	8	0.08	0.07	8	0.09	2.6
Hydrous (1 wt% H₂O)																				
LSN 51	D08	MB	45.56	1.87	13.05	1.44	9.43	0.17	15.11	8.70	2.47	1.22	0.92	99.94	1453	2.65	2.50	1425	2.54	82.1
LSN 75	D08	MB	45.72	1.88	12.97	1.42	9.41	0.16	15.12	8.77	2.34	1.23	0.91	99.93	1453	2.59	2.46	1424	2.47	80.2
LSN 54	D08	MB	45.66	1.91	13.00	1.41	9.37	0.16	15.02	8.83	2.50	1.16	0.91	99.94	1450	2.60	2.45	1423	2.49	80.8
LSN 52	D08	MB	45.55	1.90	13.50	1.41	9.32	0.16	14.86	8.90	2.31	1.11	0.92	99.93	1445	2.53	2.46	1417	2.42	78.5
LSN 56	D08	MB	45.60	1.88	13.17	1.41	9.34	0.16	14.83	8.75	2.68	1.22	0.91	99.93	1443	2.61	2.43	1419	2.51	81.4
LSN 60	D08	MB	45.60	1.86	12.95	1.43	9.66	0.16	15.35	8.33	2.54	1.16	0.90	99.94	1459	2.69	2.53	1432	2.58	83.4
LSN 76	D08	MB	45.75	1.90	13.19	1.39	9.30	0.16	14.72	8.87	2.50	1.24	0.91	99.93	1441	2.52	2.37	1414	2.42	78.5
LSN 77	D08	MB	45.97	1.89	13.13	1.38	9.25	0.16	14.69	8.91	2.41	1.23	0.91	99.93	1440	2.45	2.31	1411	2.34	76.1
LSN 59	D08	MB	45.77	1.93	13.12	1.40	9.50	0.15	15.01	8.38	2.56	1.21	0.90	99.94	1449	2.59	2.42	1421	2.47	80.2
130934	Table 1	MB	45.72	2.01	12.72	1.38	9.27	0.16	14.72	8.98	2.90	1.20	0.90	99.94	1439	2.61	2.38	1417	2.53	81.7
130933	Table 1	MB	45.70	1.97	12.59	1.41	9.55	0.16	15.19	8.58	2.71	1.18	0.90	99.93	1454	2.68	2.47	1429	2.58	83.4
LNS31	B02	PL	45.57	2.03	14.08	1.39	9.33	0.19	14.76	7.73	2.88	1.09	0.90	99.95	1440	2.59	2.42	1413	2.49	80.5
LSN 63	D08	MB	45.76	1.81	13.02	1.42	9.77	0.15	15.57	8.43	2.11	1.03	0.89	99.95	1467	2.59	2.54	1435	2.46	79.8
130931	Table 1	MB	45.71	2.00	12.40	1.41	9.61	0.16	15.16	8.49	2.90	1.23	0.89	99.94	1453	2.72	2.46	1429	2.62	84.8
LNS20	B02	MB	45.21	1.98	14.48	1.38	9.46	0.18	14.96	7.43	2.99	1.02	0.89	99.96	1445	2.71	2.56	1422	2.62	84.6
LSN 45	D08	AB	45.74	1.93	12.99	1.40	9.67	0.16	15.26	8.21	2.45	1.26	0.88	99.95	1457	2.63	2.48	1428	2.52	81.5
LSN 49	D08	AB	45.74	1.93	13.10	1.36	9.63	0.15	15.02	8.26	2.64	1.25	0.87	99.95	1449	2.61	2.43	1422	2.51	81.2
		Average	45.67	1.92	13.14	1.40	9.46	0.16	15.02	8.50	2.58	1.18	0.90	99.94	1449	2.61	2.45	1422	2.50	81.1
		Stdev	0.16	0.06	0.50	0.02	0.16	0.01	0.24	0.43	0.24	0.08	0.01	0.01	8	0.07	0.06	7	0.07	2.2

Primary basalt compositions calculated with the Fractionate-PT3 program (Lee et al., 2009) with $Fe^{3+}/\Sigma Fe = 0.13$, Mantle olivine Fo_{90}. Source of starting basalt compositions: D08, Di Bella et al. (2008);

B02, Bindi et al. (2002); Table 1, this study. Phase: PL, Paleo-Linosa; AB, Arena Bianca; MB, Monte Bandiera. Geothermobarometers: P05/A, Putirka (2005) - Model A; L09, Lee et al. (2009);

A92, Albarede (1992). Depth (z) assumes 20 km crust with 2700 kg m⁻³ density and mantle with 3300 kg m⁻³ density. Calculated P-T represent the P and T of the accumulated aggregate melt.

peridotite with an olivine composition of Fo_{90} and $Fe^{3+}/\Sigma Fe = 0.13$ (estimated following Cottrell and Kelley, 2013) for all samples that meet the criteria above ($n = 17$) are very similar, classifying as alkali basalts with $SiO_2 = 46.08 \pm 0.16$ wt%, $TiO_2 = 1.94 \pm 0.06$ wt%, $Al_2O_3 = 13.05 \pm 0.51$ wt%, $Fe_2O_3 = 1.41 \pm 0.02$ wt%, $FeO = 9.55 \pm 0.16$ wt%, $MnO = 0.16 \pm 0.01$, $MgO = 15.18 \pm 0.27$ wt%, $CaO = 8.57 \pm 0.42$ wt%, $Na_2O = 2.60 \pm 0.24$ wt%, and $K_2O = 1.19 \pm 0.08$ wt% (Table 2). Primary basalts calculated from starting basalt compositions with 1 wt% H_2O have compositions that differ by < 1% from each of these values, with the obvious exception of H_2O (0.90 ± 0.01 wt%). The olivine-liquid thermobarometer of Lee et al. (2009) provides a weighted average of the temperature and pressure of polybaric melting for the calculated primary basalts of 1449 ± 8 °C and 2.57 ± 0.09 GPa for anhydrous basalts and 1422 ± 7 °C and 2.50 ± 0.07 GPa for hydrous basalts; individual values reported in Table 2 are plotted in Fig. 7 along with the anhydrous and hydrous (116 ppm H_2O, following Salters and Stracke, 2004) peridotite solidus (Katz et al., 2003), the estimated limits of spinel and

garnet stability (following Klemme and O'Neill, 2000), and the approximate lithosphere-asthenosphere boundary (60 km; Civile et al., 2008). The calculated average pressures of segregation correspond to depths of 83.2 ± 2.6 km (anhydrous) and 81.1 ± 2.2 km (hydrous) which places their origin within the garnet-spinel transition zone, consistent with the interpretation of previous workers (Mahood and Baker, 1986; Civetta et al., 1998; Di Bella et al., 2008; Avanzinelli et al., 2014). These results suggest a mantle potential temperature between 1415 ± 7 and 1435 ± 8 °C, with calculated melt fractions of 0.019 ± 0.011 (anhydrous) to 0.027 ± 0.009 (hydrous) under those conditions (Langmuir et al., 1992; Putirka, 2005; Putirka et al., 2007; Supplementary Data 1). Also plotted in Fig. 7 are the isentropic partial melting paths for both (a) anhydrous and (b) hydrous (116 ppm H_2O) average DMM (Salters and Stracke, 2004). These paths were calculated with the pMELTS algorithm (v.5.6.1; Ghiorso et al., 2002) from the intersections of the (a) dry lherzolite solidus (Katz et al., 2003) with the 1435 °C adiabat (3.32 GPa or ~106 km, 1470 °C) and the (b) hydrous lherzolite solidus with the 1415 °C adiabat (3.62 GPa or ~116 km,
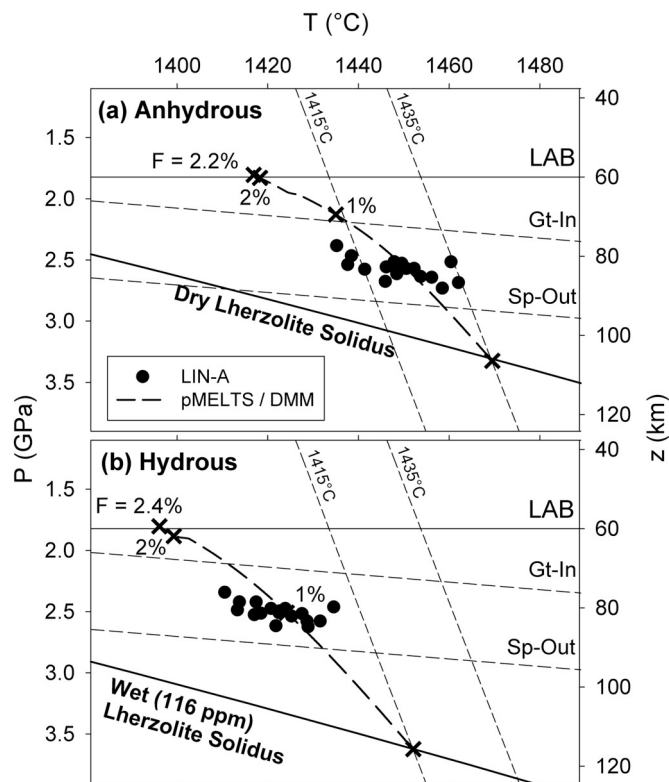
Fig. 7. FractionatePT3 (Lee et al., 2009) model results for (a) anhydrous and (b) hydrous (1 wt% H_2O) LIN-A basalts with 10 wt% < MgO < 14 wt% calculated with $Fe^{3+}/\Sigma Fe = 0.13$ and mantle Fo = 90 mol%. Plotted with these are the P-T paths for isentropic melting of (a) anhydrous and (b) hydrous (116 ppm H_2O) average depleted MORB mantle (DMM; Salters and Stracke, 2004) calculated with pMELTS (v.5.6.1) at FMQ from the intersections of the 1415° and 1430° adiabats with the (a) dry and (b) wet (116 ppm H_2O) lherzolite solidus (Katz et al., 2003). LAB: lithosphere-asthenosphere boundary. Gt-In, Sp-Out: garnet-spinel transition zone (Klemme and O'Neill, 2000). Adiabats calculated following McKenzie and Bickle (1988) and Putirka et al. (2007) (Supplementary Data 1).

1452 °C) to the base of the lithosphere (1.8 GPa, corresponding to ~60 km). Both melting models were calculated with oxygen fugacities fixed at the FMQ buffer and a step size of 50 bars (~155 m) and both predict final melt fractions of 2.2–2.5%, consistent with the value estimated from olivine-liquid thermobarometry. Model temperatures are higher than those determined for "ambient" MORB mantle ($T_P \approx 1350$ °C, 0.7–1.7 GPa; Lee et al., 2009) and similar to those determined for extension-related intraplate volcanism. Examples can be found in the Basin and Range province where the continental lithosphere has been similarly thinned, such as Owens Valley (southeastern California, USA; ~1425 °C, 60–80 km; Lee et al., 2009) and Snow Canyon (southwestern Utah, USA; ~1422 °C, 58 km; Plank and Forsyth, 2016).

Various tests have been proposed to determine the source material for basalts based on their major-element content, but these provide equivocal results for Pantelleria and Linosa. The calculated composition of primary magma for Linosa-A places it within the field of experimental partial melts of peridotite (Dasgupta et al., 2010), although the PRIMELTS3 algorithm places it in the field of partial melts of "pyroxenite" (Herzberg and Asimow, 2008). The Yang and Zhou (2013) test for mantle source composition is also equivocal: the FC3MS (wt% FeO^T/ CaO – $3MgO/SiO_2$) value of the calculated primary basalts (0.26 ± 0.07) is within the range for both peridotite (−0.07 ± 0.51) and pyroxenite (0.46 ± 0.96) partial melts. Other major-element ratios purported to flag source compositions for basalts include CaO/ Al_2O_3, K_2O/TiO_2 (Jackson and Dasgupta, 2008), and Fe/Mn (Davis

et al., 2013) and provide similarly ambiguous results: CaO/Al_2O_3 (0.65 ± 0.05) and K_2O/TiO_2 (0.61 ± 0.04) plot nearest the EM1 component and furthest from the MORB-HIMU array, inconsistent with isotopic evidence; and Fe/Mn for all basalts from both islands is 61.1 ± 5.6, which is at the proposed boundary (62) for peridotite- vs. eclogitic-derived melts. Therefore, we suggest that although these tests provide inconclusive results, they also suggest that that unenriched DMM alone is an unlikely source for LIN-A magmas specifically or for SSRZ basalts in general.

Relatively high concentrations of TiO_2 in the basalts may also support this hypothesis, as well as point to a greater role for eclogite in the source of Pantelleria basalts compared to Linosa. Following Prytulak and Elliot (2007), calculated values of Ti_8 (viz., the regressed value of TiO_2 at 8 wt% MgO) for SSRZ basalts are 1.9 (LIN-B), 2.3 (LIN-A), and 3.0 (PNL-L); these correspond to minimum concentrations (for F = 0.01 to 0.10) of TiO_2 in the mantle source of ~0.2–0.3 wt% for Linosa and ~0.3–0.5 wt% for Pantelleria compared to a range of ~0.13 wt% (DMM; Salters and Stracke, 2004) to ~0.20 wt% (PM; McDonough and Sun, 1995). Given an average concentration of 1.3 wt% TiO_2 in MORB (Sun and McDonough, 1989), these concentrations could be achieved by 5–15% recycled MORB (as eclogite) mixed with DMM for Linosa and 15–30% for Pantelleria. Additionally, the high concentrations of P_2O_5 that accompany elevated TiO_2 in the Pantelleria basalts may also indicate a higher presence of eclogite in their mantle source (Haggerty et al., 1994).

4.3. Trace element constraints on partial melting and mantle sources

The isotopic heterogeneity of the mantle is an acquired feature, but how it correlates with lithological heterogeneity is much less certain (Zindler and Hart, 1986; Dasgupta et al., 2010; Stracke, 2012). As noted in the Introduction, there is very little variability with respect to Sr and Nd isotopes in the SSRZ basalts (with the exception of the seamounts, which have high LOI [3.7 ± 2.5 wt%] and therefore may have been strongly affected by seawater weathering; Rotolo et al., 2006). Despite this apparent isotopic homogeneity with respect to Sr-Nd-He, the data clearly show several significant differences with respect to major- and trace-element compositions (and Pb isotopes; Avanzinelli et al., 2014) as well as some key similarities.

K/Nb and Nb/U ratios for Pantelleria (214 ± 38 and 49 ± 18) and Linosa (229 ± 22 and 46 ± 6) basalts are similar to global values for OIB (253 ± 71 and 47 ± 10; Hofmann et al., 1986; Halliday et al., 1995; Arevalo Jr. et al., 2009) and, combined with Sr-Nd-Pb-O isotope systematics and U-series disequilibrium, argue strongly against a significant role for crustal contamination or assimilation in the origin of these basalts (Avanzinelli et al., 2014). Pantelleria and Linosa also have similar incompatible trace element ratios for Th/U (3.3 ± 0.8 and 3.2 ± 1.6), U/Pb (0.59 ± 0.08 and 0.57 ± 0.16), Lu/Hf (0.08 ± 0.01 and 0.07 ± 0.01), and Rb/Sr (0.04 ± 0.01 and 0.05 ± 0.01) which are characteristic of HIMU end-member OIBs (Willbold and Stracke, 2006). Despite these similarities, there are several systematic differences in other trace element ratios both between and within the islands and seamounts.

Ratios of incompatible trace elements (with REE ratios normalized to CI chondrite; McDonough and Sun, 1995) are presented in Fig. 8. La_N/Yb_N is plotted against ppm La in Fig. 8a and shows a clear positive slope, strongly suggesting that variable degrees of partial melting are at least partially responsible for compositional variation in these magmas, with the higher values representing smaller melt fractions (e.g., Mahood and Baker, 1986). A plot of Sm_N/Yb_N versus La_N/Yb_N (Fig. 8b) reveals four sub-groups, which we term LIN-A (corresponding to the Linosa Trend-A described above), LIN-B (Linosa Trend-B), PNL-L (consisting of neo-Pantelleria and geochemically similar paleo-Pantelleria samples), and PNL-H (which includes both the high-Ti and P paleo-Pantelleria and the Seamount samples). The lack of collinearity between these sub-groups suggests that, although internal variation
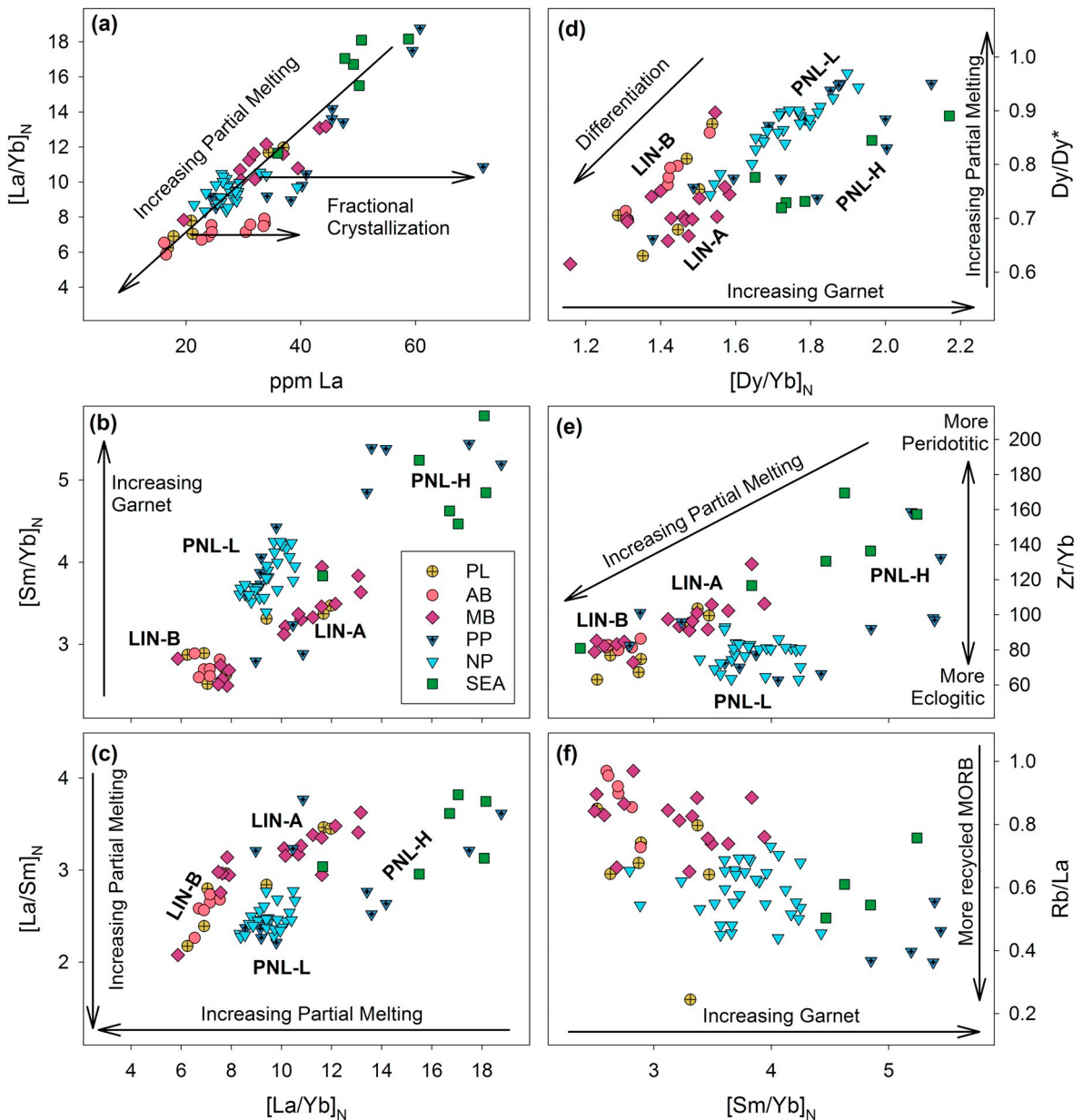
Fig. 8. Trace element ratio diagrams, with REE ratios normalized to CI Chondrite (McDonough and Sun, 1995). Dy/Dy* = Dy$_N$/[La$_N^{4/13}$·Yb$_N^{9/13}$] (Davidson et al., 2013). Units: PL, Paleo-Linosa; AB, Arena Bianca (Linosa); MB, Monte Bandiera (Linosa); PP, Paleo-Pantelleria; NP, Neo-Pantelleria; SEA, seamounts. Identified geochemical groups are labelled, as are the interpretations of the variation as discussed in the text.

within them may be attributed to varying degrees of partial melting or fractional crystallization, the differences in Sm$_N$/Yb$_N$ at a given value of La$_N$/Yb$_N$ requires different mantle sources, with the higher Sm$_N$/Yb$_N$ sub-groups sources being higher in garnet. La$_N$/Sm$_N$ is a sensitive indicator of partial melting, and therefore its overall positive correlation with La$_N$/Yb$_N$ (Fig. 8c) reinforces variation both between and within the groups as attributable to variable melt fractions; however, as with Sm$_N$/Yb$_N$, the different trends formed by the Linosa and Pantelleria groups strongly point to compositionally different mantle source regions. This is also seen in a plot of Dy/Dy* versus Dy$_N$/Yb$_N$ (Fig. 8d), which reveals three subparallel trends. In this diagram, sub-suite trends with higher Dy$_N$/Yb$_N$ also indicate a source more enriched in garnet, and the diagonal variability within each trend can be attributed to differentiation (Davidson et al., 2013). The presence of eclogite in the PNL-L source region (and for most of the paleo-Pantelleria samples in PNL-H) may be flagged by the decoupled behavior of Sm$_N$/Yb$_N$ and Zr/Yb seen in Fig. 8e. Experimental work has shown that Zr is much less

incompatible and possibly compatible in grossular-rich (eclogitic) garnet compared to pyrope-rich (peridotitic) garnet, whereas D$_{Sm}$/D$_{Yb}$ is similar in both lithologies (van Westrenen et al., 2001; Pertermann et al., 2004; Stracke and Bourdon, 2009). Avanzinelli et al. (2014) documented a negative correlation between ^{206}Pb/^{204}Pb and Rb/La within the SSRZ basalts and suggested that this ratio may be used as a tracer of recycled MORB in the source region following Willbold and Stracke (2006), who demonstrated that (Rb,Ba,K)/La ratios are systematically lower in basalts sourced from HIMU-like mantle. The negative correlation between Sm$_N$/Yb$_N$ and Rb/La in these suites (Fig. 8f) coupled with the observations above may therefore provide further evidence for eclogite in the mantle source. From these observations, we hypothesize: (1) LIN-A and LIN-B are not related by fractional crystallization processes; (2) LIN-A and LIN-B have similar Dy$_N$/Yb$_N$ and therefore may have similar mantle sources with respect to garnet, with LIN-B derived from a higher melt fraction; (3) the PNL sub-groups cannot be related via fractional crystallization; and (4) PNL-L and PNL-
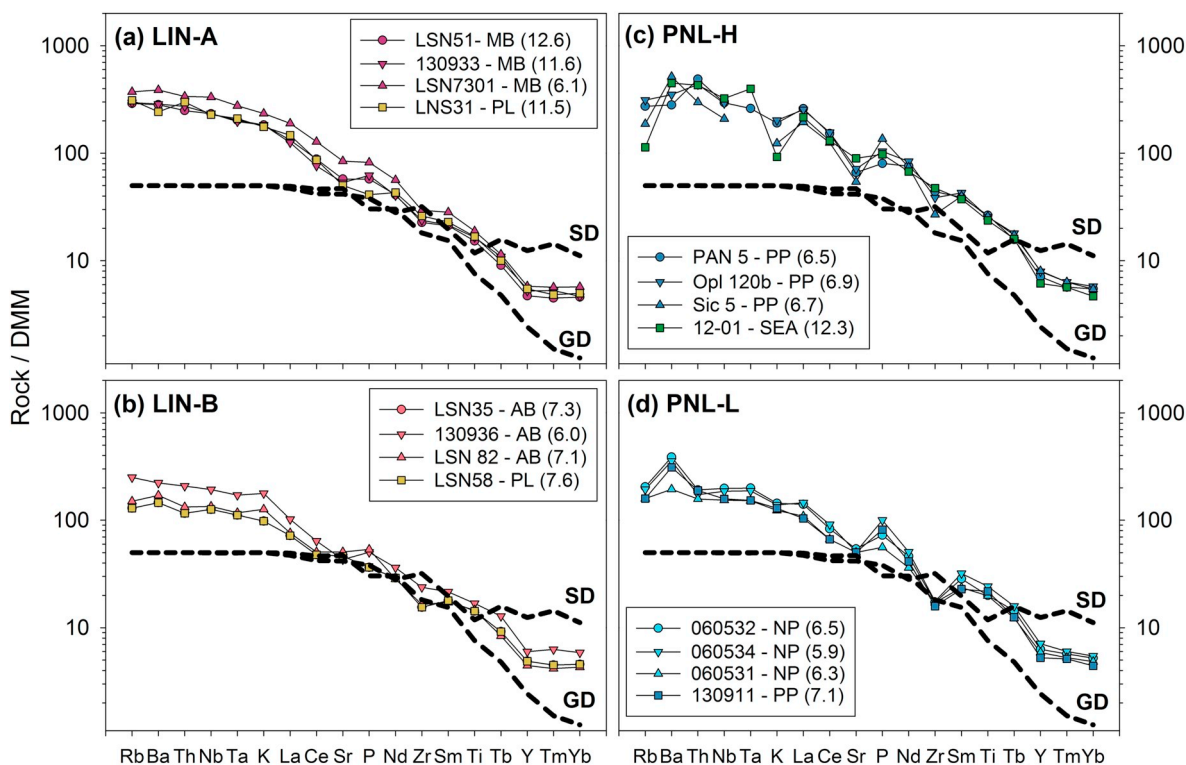
Fig. 9. Spider diagrams of representative samples (normalized to depleted MORB mantle [DMM]; Salters and Stracke, 2004) for each of the geochemical groups identified in Fig. 8. Values in parenthesis are wt% MgO of each sample. The dotted lines superimposed on each represent model non-modal fractional melts (F = 0.02) of DMM for garnet peridotite (GD) and spinel peridotite (SD) (see Supplementary Data 2).

H are either derived from different mantle sources or their differences reflect different degrees of partial melting, with the relatively lower-melt fraction PNL-H sub-suite preserving more of the signal of the more fusible, recycled material (possibly as eclogite). Due to the scarcity of data (isotope and REE data are only available for Graham Bank, Nameless Bank, and Pantelleria SE) and the lack of unaltered samples, it is more difficult to draw conclusions for the origin of the seamounts, but their very high La/Yb ratios point to melt fractions lower than Linosa (i.e., ~1%) and the generally higher values of Sm/Yb, TiO$_2$, and P$_2$O$_5$ for Graham Bank and Nameless Bank may be attributed to magma generation away from the rift grabbens and beneath thicker lithosphere (cf. Niu et al., 2011).

Spider diagrams of representative analyses from each of the sub-groups ordered by increasing compatibility in oceanic basalts (following Sun and McDonough, 1989) and normalized to DMM (Salters and Stracke, 2004) are presented in Fig. 9. These are plotted with the results of 2% (F = 0.02) non-modal fractional melting of depleted garnet peridotite (GD) and spinel peridotite (SD) (see Supplementary Data 2 for details.) The model results for partial melting of DMM form patterns very similar to those formed by all four sub-groups. Most notably, all groups form trends that run subparallel to the model results with excellent fits for the LREE and more compatible elements, consistent with a similar origin by small degrees of partial melting of depleted peridotite in the spinel-garnet transition zone followed by fractional crystallization. However, several notable anomalies require additional explanation: (1) in addition to DMM, the source regions for all four groups require a source component enriched in LILE; (2) a positive P anomaly is present in both PNL groups, and is especially prominent in the PNL-H lavas; (3) PNL suites are characterized by relatively high Ti and low Zr; and (4) the strong variability in PNL-H LILE contents and ratios strongly suggests that several different components must be present in the source region for these diverse magmas which clearly must not be related by either partial melting or fractional crystallization processes.

Therefore, we posit: (1) all magmas originate in the spinel-garnet transition zone from a source region dominated by DMM peridotite (Civetta et al., 1998; Neave et al., 2012; Avanzinelli et al., 2014); (2) first-order differences between Pantelleria and Linosa/Seamounts are due to a greater amount of lithologically-enriched and possibly eclogitic material mixed with peridotite in the former (cf. Avanzinelli et al., 2014); (3) differences between the Seamounts, LIN-A, and LIN-B are due to variable degrees of partial melting, with the Seamounts and Linosa-B being derived from the lowest and highest degrees of partial melting respectively; (4) compositional diversity within the paleo-Pantelleria suite must reflect the presence of additional diverse components in the mantle source and indicate mantle heterogeneity at the inter-island (10s of km) scale beneath Pantelleria (cf. Civetta et al., 1998); and (5) compositional homogeneity in the LIN-B and PNL-L is probably due to homogenization in high-level magma reservoirs (see Fig. 6), which obfuscates the variability from partial melting seen in LIN-A and heterogeneity observed in PNL-H (e.g., McGee and Smith, 2016). In most PNL-L samples and some PNL-H samples there is also a positive Ba anomaly which may be the result of a small amount of assimilation of high-Ba alkali feldspar cumulate rock at Pantelleria (White et al., 2012; Wolff, 2017).

4.4. Trace element models of partial melting

Whole-rock REE concentrations, along with major- and selected trace-element concentrations, were used to model the conditions of partial melting beneath Pantelleria and Linosa by means of the INVMEL program (McKenzie and O'Nions, 1991, 1995, 1998) as modified by White et al. (1992). This program inverts REE geochemical data to find the best-fit relationship between melt fraction and depth utilizing the partitioning behavior of a full suite of REE in mantle phases (Neave et al., 2012). It does this by running an initial forward non-modal fractional melting model with trial parameters, predicting the weighted average composition of the fractional melt, calculating the root-mean
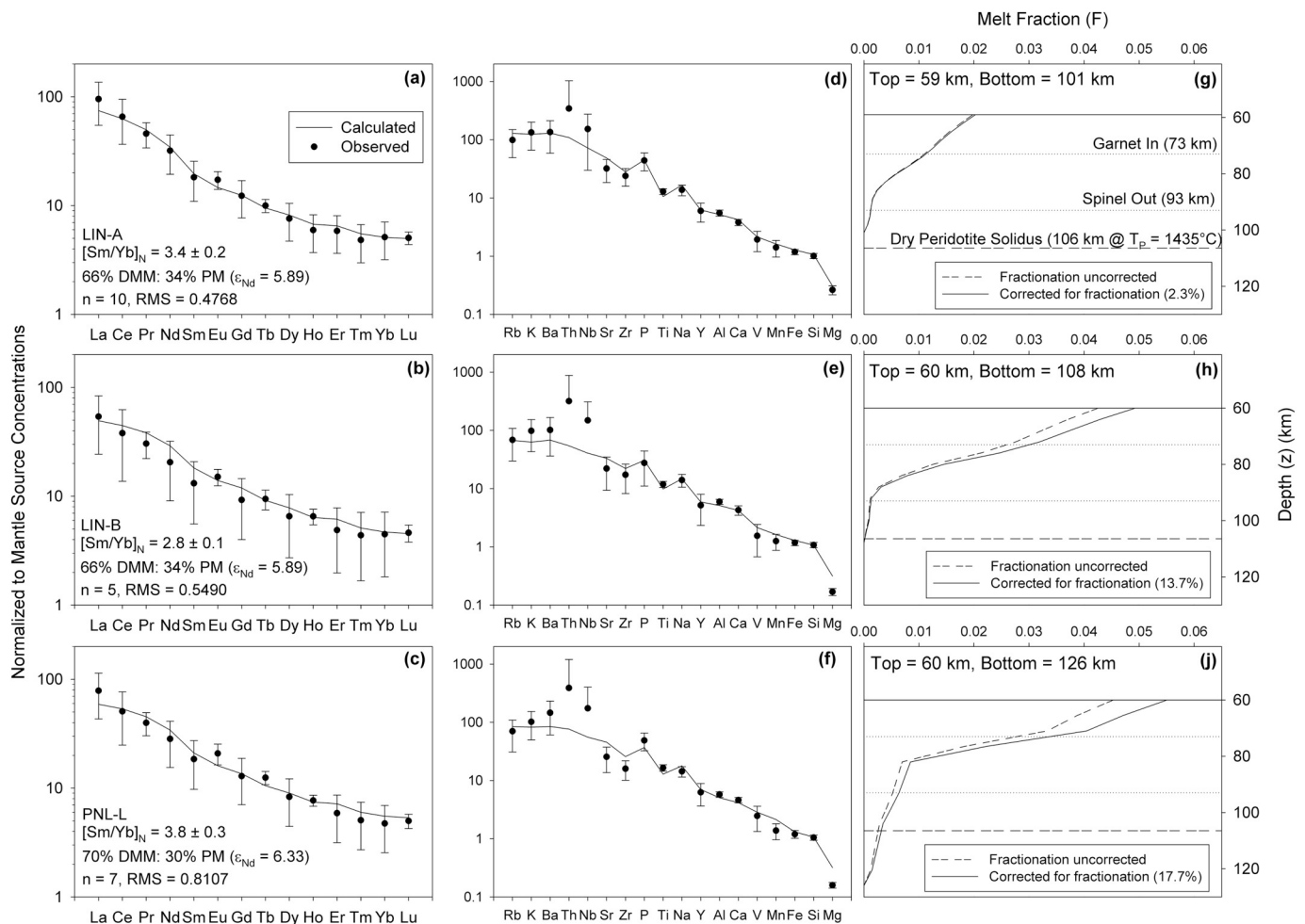
Fig. 10. Results of rare-earth element inverse modelling (a, b, c), major- and trace-element forward model predictions (d, e, f), and calculated melting curves (g, h, j) for LIN-A, LIN-B, and PNL-L. Chondrite-normalized Sm/Yb values represent the average of the sample set (n = total number of samples used in the model). RMS = root mean square error.

square (RMS) error between the predicted and observed calculations, and then adjusting the melt depth and degree curve to iteratively minimize the error. After the best-fit parameters producing the least misfit have been determined, a final forward non-modal fractional melting model is run through the remaining major- and trace-element data to evaluate the robustness of fit. Results are considered acceptable if RMS < 1 and the melting curve is relatively smooth. The program also estimates the quantity of olivine and clinopyroxene fractionation (F), and the final melt fraction is adjusted by multiplication by $1/(1-F)$. The mantle source is set with the ε_{Nd} parameter, which calculates a mixture of DMM (ε_{Nd} = +10, 0.815 ppm Nd) and bulk silicate earth ("Primitive" Mantle, PM: ε_{Nd} = 0, 1.08 ppm Nd) (McKenzie and O'Nions, 1991, 1998). The latter component does not necessarily represent primitive mantle or deep mantle plume material, but serves as a proxy for various enriched components such as recycled oceanic lithosphere that are well-mixed with peridotite and whose compositions are not well-constrained (Gibson and Geist, 2010). Model mineral proportions and chemical composition of DMM and PM sources are from McKenzie and O'Nions (1991, 1995), with the mineral-liquid trace element partition coefficients compiled by Gibson and Geist (2010) (see Supplementary Data 2).

Inversion models for the three subgroups that are plausibly cogenetic (LIN-A, LIN-B, and PNL-L) are presented in Fig. 10. Average ε_{Nd} values from Linosa (5.89) were used to set the mantle source region for both LIN-A and LIN-B, which corresponds to a mix of 66% DMM and 34% PM; the average ε_{Nd} for Pantelleria used in the models (6.33) was

used to set the mantle source region for PNL-L, which corresponds to a mix of 70% DMM and 30% PM. Models were calculated with the garnet-spinel transition zone fixed at 73–93 km (based on a mantle potential temperature of 1435 °C; Klemme and O'Neill, 2000), while the top and bottom of the melting column were allowed to vary. All models fit the observed REE data well and within 1σ (Fig. 10a, b, c) with the exception of Eu in the PNL-L model, which is slightly higher. In the forward models (Fig. 10d, e, f), the results also fit the observed major and trace element data well, with a few notable exceptions: observed Th and Nb values are ubiquitously higher (68–83% and 53–73% respectively) than model results for both islands, but within error, and observed Sr and Zr values are lower (50% and 17–28% respectively) than model results for Linosa, but within 1σ and below that at Pantelleria. The models with the best fits have the tops of the melting columns at 59–60 km and the bases of the melting columns at 101 km (LIN-A; RMS = 0.4768), 108 km (LIN-B; RMS = 0.5490) and 126 km (PNL-L; RMS = 0.8107) (Fig. 10g, h, i). The top values are consistent with the geophysical evidence for the ~60 km lithosphere-asthenosphere boundary in the SSRZ (Della Vedova et al., 1995; Civile et al., 2008). The bottom of the melting column for both LIN-A and LIN-B lie at or slightly below of the intersection of the 1435 °C mantle adiabat and the dry peridotite solidus (~106 km; depths calculated assuming densities of 2700 kg m^{-3} for the [20 km thick] crust and 3300 kg m^{-3} for the mantle). The bottom of the melting column for PNL-L lies between the peridotite solidus and the intersection of the 1435 °C adiabat with the G2 pyroxenite solidus (~137 km; Pertermann and Hirschmann, 2003).

It is important to note that the results of these models are relative rather than absolute—for instance, if the garnet-spinel transition zone is fixed at 75–95 km for a mantle potential temperature of 1450 °C, identical results are obtained for a top and bottom 3 km deeper (viz., 62–63 km top and 104–124 km bottom), although the intersections of the adiabats with the solidii would be 4–6 km deeper (dry peridotite: 112 km, pyroxenite: 141 km).

These results suggest that the Linosa basalts are produced by variable degrees of partial melting (~2% for LIN-A and ~5% for LIN-B) of similar peridotitic asthenosphere. The presence in each diagram of a small, low-fraction melt "tail" at the base of the melting column may flag the presence of a minor amount of lithologically enriched and possibly water-rich material (Gibson and Geist, 2010). This "tail" is deeper, much larger, and more prominent in the PNL-L melting curve, which supports the hypothesis that the mantle source beneath Pantelleria is much more enriched in incompatible trace elements. Likewise, the predicted melting column extends below the peridotite solidus to 126 km at T_P = 1435 °C, consistent with early melting of pyroxenitic material, which is more fusible than peridotite and under these conditions would begin melting between 115 and 130 km (Hirschmann and Stolper, 1996; Kogiso et al., 1998; Pertermann and Hirschmann, 2003). The model for PNL-L also suggests a fraction of partial melting similar to LIN-B (~5.5%). The INVMEL model was applied to Pantelleria basalts by Neave et al. (2012), who reported similar results (melting across 100–60 km with the garnet-spinel transition zone between 90 and 70 km, corresponding to a mantle potential temperature of ~1400 °C) but with a much lower melt fraction (~1.7%). This lower value is likely due to the inclusion of high-La/Yb PNL-H samples with the PNL-L basalts and their use of a primitive mantle source in their model.

5. Summary

Geochemical modelling of basaltic magmatism supports previous geophysical models for the structure of the lithosphere in the Strait of Sicily, suggesting the lithosphere-asthenosphere boundary beneath the islands occurs at ~60 km, with the Moho beneath Linosa at ~24–25 km and high-level magma reservoirs occurring at the top of the crystalline basement between 4 and 8 km. Basalts on both islands fractionated in high-level chambers, although the more primitive magmas erupted on Linosa fractionated from chambers emplaced at the Moho. The asthenosphere underneath the SSRZ is characterized by mantle potential temperatures of 1415–1435 °C and consists of depleted MORB lherzolite well-mixed with recycled MORB lithosphere (as eclogite/garnet pyroxenite), in agreement with Avanzinelli et al. (2014). For the most primitive basalts on Linosa (termed LIN-A and primarily represented by the younger [530 ka] Monte Bandiera volcanics), there is good agreement between major-element models (FRACTIONATE-PT3; Lee et al., 2009), thermodynamic models of isentropic mantle melting (pMELTS; Ghiorso et al., 2002), and trace element inversion models (INVMEL; McKenzie and O'Nions, 1991, 1995). The models collectively suggest that these basalts are the result of ~2% partial melting of a mantle source dominated by depleted MORB mantle (DMM) lithologically enriched with a relatively small fraction of recycled MORB (as eclogite/garnet pyroxenite). The older, generally more evolved basalts on Linosa (termed LIN-B and primarily represented by the older [700 ka] Arena Bianca volcanics) formed from a higher degree of partial melting (~5%) of the same mantle source. In comparison with Linosa, the geochemistry of the basalts on Pantelleria provide evidence that they were sourced from DMM-dominated mantle lithologically enriched with a much larger fraction of recycled MORB and possibly other components; evidence for this includes higher TiO_2 and P_2O_5 at a given MgO compared to Linosa, higher Sm/Yb and Dy/Yb at a given La/Yb coupled with a lower Zr/Yb, and higher Rb/La coupled with higher $^{206}Pb/^{204}Pb$ ratios (cf. Avanzinelli et al., 2004). The results of INVMEL modelling also indicate that the Pantelleria basalts cannot be derived from a peridotite-only source. We hypothesize that greater melt productivity at Pantelleria and its ability to drive felsic magmatism compared to the remainder of the SSRZ may simply be due to the presence of more fusible mantle beneath the island, indicating mantle heterogeneity at a relatively short length-scale in the SSRZ.

Declaration of competing interest

The authors declare that they have no known competing financial interests or personal relationships that could have appeared to influence the work reported in this paper.

Appendix A. Supplementary data

Supplementary data to this article can be found online at https://doi.org/10.1016/j.chemgeo.2020.119650.

References

Albarede, F., 1992. How deep do common basaltic magmas form and differentiate? J. Geophys. Res. 97, 10997–11009. https://doi.org/10.1029/91JB02927.

Aissi, M., Flovere, M., Würtz, M., 2015. Seamounts and seamount-like structures of Sardinia Channel, Strait of Sicily, Ionian Sea, and Adriatic Sea. In: Würtz, M., Rovere, M. (Eds.), Atlas of the Mediterranean Seamounts and Seamount-like Structures. International Union for Conservation of Nature (IUCN), Gland, Switzerland and Málaga, Spain, pp. 187–225. https://doi.org/10.2305/ICUN.CH.2015.07.en.

Arevalo Jr., R., McDonough, W.F., Luong, M., 2009. The K/U ratio of the silicate Earth: Insights into mantle composition, structure, and thermal evolution. Earth Planet. Sci. Lett. 278, 361–369 (doi: 1016/j.espl.2008.12.023).

Argnani, A., Torelli, L., 2001. The Pelagian Shelf and its graben system (Italy/Tunisia). In: Ziegler, P.A., Cavazza, W., Robertson, A.H.F., Crasquin-Soleau, S. (Eds.), Peri-Tethys Memoir 6: Peri-Tethyan Rift/Wrench Basins and Passive Margins. Mém. Mus. Natl. Hist. Nat 186. pp. 529–544.

Asimow, P.D., Ghiorso, M.S., 1998. Algorighmic modifications extending MELTS to calculated subsolidus phase relations. Amer. Miner. 83, 1127–1131. https://doi.org/10.2138/am-1998-9-1022.

Avanzinelli, R., Bindi, L., Menchetti, S., Conticelli, S., 2004. Crystallization and genesis of peralkaline magmas from Pantelleria Volcano, Italy: an integrated petrological and crystal-chemical study. Lithos 73, 41–69. https://doi.org/10.1016/j.lithos.2013.10.008.

Avanzinelli, R., Braschi, E., Marchionni, S., Bindi, L., 2014. Mantle melting in within-plate continental settings: Sr-Nd-Pb and U-series isotope constraints in alkali basalts from the Sicily Channel (Pantelleria and Linosa Islands, Southern Italy). Lithos 188, 113–129. https://doi.org/10.1016/j.lithos.2013.008.

Beccaluva, L., Colantoni, P., Di Girolamo, P., Savelli, C., 1981. Upper-Miocene submarine volcanism in the Strait of Sicily (Banco senza Nome). Bull. Volcanol. 44, 573–581. https://doi.org/10.1007/BF02600587.

Bellani, S., Calore, C., Grassi, S., Squarci, P., 1995. Thermal Prospecting in Pantelleria Island (Sicily Channel, Italy). 2. World Geothermal Congress, Firenze, pp. 767–770. https://doi.org/10.13140/RG.2.1.1040.0165. 1995.

Berrino, G., Capuano, P., 1995. Gravity anomalies and structures at the island of Pantelleria. Acta Vulcanol. 7, 19–26.

Bindi, L., Tasselli, F., Olmi, F., Peccerillo, A., Menchetti, S., 2002. Crystal chemistry of clinopyroxenes from Linosa Volcano, Sicily Channel, Italy: implications for modelling the magmatic plumbing system. Mineral. Mag. 66, 953–968. https://doi.org/10.1180/0026461026660070.

Calanchi, N., Colantoni, P., Rossi, P.L., Saitta, M., Serri, G., 1989. The Strait of Sicily continental rift systems: physiography and petrochemistry of the submarine volcanic centers. Mar. Geol. 87, 55–83. https://doi.org/10.1016/0025-3227(89)90145-X.

Catalano, S., De Guidi, G., Lanzafame, G., Monaco, C., Tortorici, L., 2009. Late Quaternary deformation on the island of Pantelleria: new constraints for the recent tectonic evolution of the Sicily Channel Rift (southern Italy). J. Geodyn. 48, 75–82.

https://doi.org/10.1016/j.jog.2009.06.005.

Cavallaro, D., Coltelli, M., 2019. The Graham Volcanic Field offshore southwestern Sicily (Italy) revealed by high-resolutioon seafloor mapping and ROV images. Front. Earth Sci. 7, 311. https://doi.org/10.3389/feart.2019.00311.

Civetta, L., D'Antonio, M., Orsi, G., Tilton, G.R., 1998. The geochemistry of volcanic rocks from Pantelleria Island, Sicily Channel: petrogenesis and characteristics of the mantle source region. J. Petrol. 39, 1453–1491. https://doi.org/10.1093/petrology/39.8.1453.

Civile, D., Lodolo, E., Tortorici, L., Lanzafame, G., Brancolini, G., 2008. Relationships between magmatism and tectonics in a continental rift: the Pantelleira Island region (Sicily Channel, Italy). Mar. Geol. 251, 32–46. https://doi.org/10.1016/j.margeo.2008.01.009.

Civile, D., Lodolo, E., Accettella, D., Geletti, R., Ben-Avraham, Z., Deponte, M., Facchin, L., Ramella, R., Romeo, R., 2010. Tetctonophysics. 490, 173–183. https://doi.org/10.1016/j.tecto.2010.05.008.

Class, C., Goldstein, S.L., 2005. Evolution of helium isotopes in the earth's mantle. Nature 436, 1107–1112. https://doi.org/10.1038/nature03930.

Coltelli, M., Cavallaro, D., D'Anna, G., D'Alessandro, A., Grassa, F., Mangano, G., Patanè, D., Gresta, S., 2016. Exploring the submarine Graham Bank in the Sicily Channel. Ann. Geophys. 59 (2), S0208. https://doi.org/10.4401/ag-6929.

Conte, A.M., Martorelli, E., Calarco, M., Sposato, A., Perinelli, C., Coltelli, M., Chiocci, F.L., 2014. The 1891 submarine erupton offshore Pantelleria Island (Sicily Channel, Italy): identification of the vent and characterization of products and eruptive style. Geochem. Geophys. Geosyst. 15, 2555–2574. https://doi.org/10.1002/2014GC005238.

Cottrell, E., Kelley, K.A., 2013. Redox heterogeneity in Mid-Ocean Ridge Basalts as a function of mantle source. Science 340, 1314–1317. https://doi.org/10.1126/science.1233299.

Dasgupta, R., Jackson, M.G., Lee, C.-T.A., 2010. Major element chemistry of ocean island basalts – conditions of mantle melting and heterogeneity of mantle source. Earth Planet. Sci. Lett. 289, 377–392. https://doi.org/10.1016/j.espl.2009.11.027.

Davidson, J., Turner, S., Plank, T., 2013. Dy/Dy*: variations arising from mantle sources and petrogenetic processes. J. Petrol. 54, 525–537. https://doi.org/10.1093/petrology/egs076.

Davis, F.A., Humayun, M., Hirschmann, M.M., Cooper, R.S., 2013. Experimentally determined mineral/melt partitioning of first-row transition elements (FRTE) during partial melting of peridotite at 3 GPa. Geochim. Cosmochim. Acta 104, 232–260. https://doi.org/10.1016/j.gca.2012.11.009.

Della Vedova, B., Lucazeau, F., Pasquale, V., Pellis, G., Verdoya, M., 1995. Heat flow in the tectonic provinces crossed by the southern segment of the European Geotraverse. Tectonophysics 244, 57–74 (doi: 10.106/0040-1951(94)00217-W).

Di Bella, M., Russo, S., Petrelli, M., Peccerillo, A., 2008. Origin and evolution of the Pleistocene magmatism of Linosa Island (Sicily Channel, Italy). Eur. J. Mineral. 20, 587–601. https://doi.org/10.1127/0935-1221/2008/0020-1832.

Esperança, S., Crisci, G.M., 1995. The island of Pantelleria: a case for the development of DMM-HIMU isotopic compositions in a long-lived extensional setting. Earth Planet. Sci. Lett. 136, 167–182. https://doi.org/10.1016/0012-821X(95)00178-F.

Fouré, E., Allard, P., Jean-Baptiste, P., Cellura, D., Parello, F., 2012. ^{3}He/^{4}He ratio in olivines from Linosa, Ustica, and Pantelleria Islands (Southern Italy). J. Geol. Res. https://doi.org/10.1155/2012/723839.

Fulignati, P., Malfitano, G., Sbrana, A., 1997. The Pantelleria caldera geothermal system: data from the hydrothermal minerals. J. Volcanol. Geotherm. Res. 75, 251–270. https://doi.org/10.1016/S0377-0273(96)00066-2.

Gemmellaro, C., 1831. Relazione dei fenomeni del nuovo vulcano sorto dal mare fra la costa di Sicilia e l'isola di Pantelleria nel mese di luglio 1831. Atti dell'Accademia Gioenia di Scienze Naturali in Catania 8, 271–298.

Ghiorso, M.S., Sack, R.O., 1995. Chemical mass transfer in magmatic processes. IV. A revised and internally consistent thermodynamic model for rthe interpolation and extrapolation of liquid-solid equilibria in magmatic systems at elevated temperatures and pressures. Contrib. Mineral. Petrol. 119, 197–212. https://doi.org/10.1007/BF00307281.

Ghiorso, M.S., Hirschmann, M.M., Reiners, P.W., Kress, V.C., 2002. The pMELTS: a revison of MELTS aimed at improving calculation of phase relations and major element partitioning involved in partial melting of the mantle at pressures up to 3 GPa. Geochem. Geophys. 3 (5). https://doi.org/10.1029/2001GC000217.

Gibson, S.A., Geist, D., 2010. Geochemical and geophysical estimates of lithospheric thickness variation beneath Galápagos. Earth Planet. Sci. Lett. 300, 275–286. https://doi.org/10.1016/j.epsl.2010.10.002.

Gualda, G.A.R., Ghiorso, M.S., Lemons, R.V., Carley, T.L., 2012. Rhyolite-MELTS: a modified calibration of MELTS optimized for silica-rich, fluid-bearing magmatic systems. J. Petrol. 53, 875–890. https://doi.org/10.1093/petrology/egr080.

Haggerty, S.E., Fung, A.T., Burt, D.M., 1994. Apatite, phosphorous and titanium in eclogitic garnet from the upper mantle. Geophys. Res. Lett. 21, 1699–1702. https://doi.org/10.1029/94GL01001.

Halliday, A.N., Lee, D.-C., Tommasini, S., Davies, G.R., Paslick, C.R., Fitton, J.G., James, D.E., 1995. Incompatible trace elements in OIB and MORB and source enrichment in the sub-oceanic mangle. Earth Planet. Sci. Lett. 113, 379–395. https://doi.org/10.1016/0012-821X(95)00097-V.

Herzberg, C., Asimow, P.D., 2008. PRIMELT3 MEGA.XLSM software for primary magma calculation: Peridotite primary magma MgO contents from the liquidus to the solidus. Geochem. Geophys. 16, 563–578. https://doi.org/10.1002/2014GC00563.

Hirschmann, M.M., Stolper, E.M., 1996. A possible role for garnet pyroxenite in the origin of the "garnet signature" in MORB. Contrib. Mineral. Petrol. 124, 185–208. https://doi.org/10.1007/s004100050184.

Hofmann, A.W., Jochum, K.P., Seufert, M., White, W.M., 1986. Nb and Pb in oceanic basalts: new constraints on mantle evolution. Earth Planet. Sci. Lett. 79, 33–45.

https://doi.org/10.1016/0012-821X(86)90038-5.

Irvine, T.N., Baragar, W.R.A., 1971. A guide to the chemical classification of the common volcanic rocks. Can. J. Earth Sci. 8, 523–548. https://doi.org/10.1139/e71-055.

Jackson, M.G., Dasgupta, R., 2008. Compositions of HIMU, EM1, and EM2 from global trends between radiogenic isotopes and major elements in oceanic island basalts. Earth Planet. Sci. Lett. 276, 175–186. https://doi.org/10.1016/j.espl2008.09.023.

Katz, R.F., Spiegelman, M., Langmuir, C.H., 2003. A new parameterization of hydrous manltle melting. Geochem. Geophys. 4 (9), 1073. https://doi.org/10.1029/2002GC000433.

Kelly, J.T., Carey, S., Pistolesi, M., Rosi, M., Croff-Bell, K.L., Roman, C., Marani, M., 2014. Exploration o the 1891 Foerstner submarine vent site (Pantellria, Italy): insights into the formation of basaltic balloons. Bull. Volc. 76, 844. https://doi.org/10.1007/s00445-014-0844-4.

Klemme, S., O'Neill, H.StC., 2000. The near-solidus transition from garnet lherzolite to spinel lherzolite. Contrib. Mineral. Petrol. 138, 237–248. https://doi.org/10.1007/s004100050560.

Kogiso, T., Hirose, K., Takahashi, E., 1998. Melting experiments on homogenous mixtures of peridotitee and basalt: application to the genesis of ocean island basalts. Earth Planet. Sci. Lett. 162, 45–61. https://doi.org/10.1016/S0012-821X(98)00156-3.

Langmuir, C.H., Klein, E.M., Plank, T., 1992. Petrological systematics of mid-ocean ridge basalts: constraints on melt generation beneath ocean ridges. In: Morgan, J.P., Blackman, D.K., Sinton, J.M. (Eds.), Mantle Flow and Melt Generation at Mid-ocean Ridges. Geophys. Monogr. Ser 71. AGU, Washington D.C, pp. 183–280. https://doi.org/10.1029/GM071p0183.

Lanzafame, G., Rossi, P.L., Tranne, C.A., Lanti, E., 1994. Carta geologica dell'isola di Linosa. 1:5000. Società Elaborazioni Cartografiche, Firenze.

Le Maitre, R.W. (Ed.), 2002. Igneous Rocks, a Classification and Glossary of Terms: Recommendations of the International Union of Geological Sciences Subcomision on the Systematics of Igneous Rocks, 2nd ed. Cambridge University Press (236 p).

Lee, C.-T.A., Luffi, P., Plank, T., Dalton, H., Leeman, W.P., 2009. Constraints on the depths and temperatures of basaltic magma generation on Earth and other terrestrial planets using new thermobarometers for mafic magmas. Earth Planet. Sci. Lett. 279, 20–33. https://doi.org/10.1016/j.espl.2008.12.020.

Lodolo, E., Zampa, L., Civile, D., 2019. The Graham and Terrible volcanic province (NW Sicilian Channel): gravimetric constraints for the magmatic manifestations. Bull. Volcanol. 81, 17. https://doi.org/10.1007/s00445-019-1274-0.

Mahood, G.A., Baker, D.R., 1986. Experimental constraints on depths of fractionation of mildly alkalic basalts and associated felsic rocks: Pantelleria, Strait of Sicily. Contrib. Mineral. Petrol. 93, 251–264. https://doi.org/10.1007/BF00371327.

Mahood, G.A., Hildreth, W., 1986. Geology of the peralkaline volcano at Pantelleria, Strait of Sicily. Bull. Volcanol. 48, 143–172. https://doi.org/10.1007/BF01046548.

Martinelli, M., Bistacchi, A., Balsamo, F., Meda, M., 2019. Late Oligocene to Pliocene extension in the Maltese islands and implications for geodynamics of the Pantelleria Rift and Pelagian Platform. Tectonics 38, 3394–3415. https://doi.org/10.1029/2019TC005627.

McDonough, W.F., Sun, S.-s., 1995. The composition of the earth. Chem. Geol. 120, 223–253.

McGee, L.E., Smith, I.E.M., 2016. Interpreting chemical compositions of small scale basaltic systems: a review. J. Volcanol. Geotherm. Res. 325, 45–60. https://doi.org/10.1016/j.volgeores.2016.06.007.

McKenzie, D., Bickle, M.J., 1988. The volume and composition of melt generated by extension of the lithosphere. J. Petrol. 29, 625–679. https://doi.org/10.1093/petrology/29.3.625.

McKenzie, D., O'Nions, R.K., 1991. Partial melt distributions from inverstion of rare earth element concentrations. J. Petrol. 32, 1021–1091. https://doi.org/10.1093/petrology/32.5.1021.

McKenzie, D., O'Nions, R.K., 1995. The source regions of ocean island basalts. J. Petrol. 36, 133–159. https://doi.org/10.1093/petrology/36.1.133.

McKenzie, D., O'Nions, R.K., 1998. Melt production beneath oceanic islands. Phys. Earth Planet. Inter. 107, 143–182. https://doi.org/10.1016/S0031-9201(97)00132-5.

Neave, D.A., Fabbro, G., Herd, R.A., Petrone, C.M., Edmonds, M., 2012. Melting, differentiation and degassing at the Pantelleria Volcano, Italy. J. Petrol. 53, 637–663. https://doi.org/10.1093/petrology/egr074.

Niu, Y., O'Hara, M.J., 2009. MORB mantle hosts the missing Eu (Sr, Nb, Ta, and Ti) in the continental crust: New perspectives on crustal growth, crust-mantle differentiation and chemical signature of the oceanic upper mantle. Lithos 112, 1–17. https://doi.org/10.1016/j.lithos.2008.12.009.

Niu, Y., Wilson, M., Humphrey, E.R., O'Hara, M.J., 2011. The origin of intra-plate ocean island basalts (OIB): the lid effect and its geodynamic implications. J. Petrol. 52, 1443–1468. https://doi.org/10.1093/petrology/egr030.

O'Hara, M.J., 1968. The bearing of phase equilibria studies in synthetic and natural systems on the origin and evolution of basic and ultrabasic rocks. Earth Sci. Rev. 4, 69–133. https://doi.org/10.1016/0012-8252(68)90147-5.

Parello, F., Allard, P., D'Alessandro, W., Federico, C., Jean-Baptiste, P., Catani, O., 2000. Isotope geochemistry of Pantelleria volcanic fluids, Sicily Channel rift: a mantle volatile end-member for volcanism in southern Europe. Earth Planet. Sci. Lett. 180, 325–339. https://doi.org/10.1016/S0012-821X(00)00183-7.

Parker, D.F., White, J.C., 2008. Large-scale alkalic magmatism associated with the Buckhorn caldera, Trans-Pecos Texas, USA: comparison with Pantelleria, Italy. Bull. Volcanol. 70, 403–415. https://doi.org/10.1007/s00445-007-0145-2.

Pearce, T.H., 1968. A contribution to the theory of variation diagrams. Contrib. Mineral. Petrol. 19, 142–157. https://doi.org/10.1007/BF00635485.

Pertermann, M., Hirschmann, M.M., 2003. Partial melting experiments on a MORB-like pyroxenite between 2 and 3 GPa: constraints on the presence of pyroxenite in basalt source retions from solidus location and melting rate. J. Geophys. Res. 108 (B2), 2125. https://doi.org/10.1029/2000JB000118.

Pertermann, M., Hirschmann, M.M., Hametner, K., Günther, D., Schmidt, M.W., 2004. Experimental determination of trace element partitioning between garnet and silica-rich liquid during anhydrous melting of MORB-like eclogite. Geochem. Geophys. 5 (5), Q05A01. https://doi.org/10.1029/2003/GC000638.

Plank, T., Forsyth, D.W., 2016. Thermal structure and melting conditions in the mantle beneath the Basin and Range province from seismology and petrology. Geochem. Geophys. 17, 1312–1338. https://doi.org/10.1002/2015GC006205.

Prytulak, J., Elliot, T., 2007. TiO$_2$ enrichment in ocean island basalts. Earth Planet. Sci. Lett. 263, 388–403. https://doi.org/10.1016/j.epsl.2007.09.015.

Putirka, K.D., 2005. Mantle potential temperatures at Hawaii, Iceland, and the mid-ocean ridge system, as inferred from olivine phenocrysts: evidence for thermally driven mantle plumes. Geochem. Geophys. 6 (5), Q05L08. https://doi.org/10.1029/2005GC000915.

Putirka, K.D., Perfit, M., Ryerson, F.J., Jackson, M.G., 2007. Ambient and excess mantle termperatures, olivine thermometry, and active vs. passive upwelling. Chem. Geol. 241, 177–206. https://doi.org/10.1016/j.chemgeo.2007.01.014.

Romagnoli, C., Belvisi, V., Innangi, S., Di Martino, G., Tonielli, R., 2020. New insights on the evolution of the Linosa volcano (Sicily Channel) from the study of its submarine portions. Mar. Geol. 419, 106060. https://doi.org/10.1016/j.margeo.2019.106060.

Rossi, P.L., Tranne, C.A., Calanchi, N., Lanti, E., 1996. Geology, stratigraphy and volcanological evolution of the island of Linosa (Sicily Channel). Acta Vulcanol. 8, 73–90.

Rotolo, S.G., Castorina, F., Cellura, D., Pompilio, M., 2006. Petrology and geochemistry of submarine volcanism in the Sicily Channel rift. J. Geol. 114, 355–365. https://doi.org/10.1086/501223.

Russell, J.K., Nicholls, J., 1988. Analysis of petrologic hypotheses with Pearce element ratios. Contrib. Mineral. Petrol. 99, 25–35. https://doi.org/10.1007/BF00399362.

Salters, V.J.M., Stracke, A., 2004. Composition of depleted mantle. Geochem. Geophys. 5 (5), Q05004. https://doi.org/10.1029/2003GC000597.

Scaillet, S., Vita-Scaillet, G., Rotolo, S.G., 2013. Millennial-scale phase relationships between ice-core and Mediterranean marine records: insights from high-precision ^{40}Ar/^{39}Ar dating of the Green Tuff of Pantelleria, Sicily Strait. Quat. Sci. Rev. 78, 141–154. https://doi.org/10.1016/j.quascirev.2013.08.008.

Stracke, A., 2012. Earth's homogenous mantle: a product of convection-driven interacton between crust and mantle. Chem. Geol. 330–331, 274–299. https://doi.org/10.1016/j.chemgeo.2012.08.007.

Stracke, A., Bourdon, B., 2009. The importance of melt extraction for tracing mantle heterogeneity. Geochim. Cosmochim. Acta 73, 218–238. https://doi.org/10.1016/j.gca.2008.10.015.

Sun, S.-s., McDonough, W.F., 1989. Chemical and isotopic systematics of oceanic basalts: implications for mantle composition and processes. Geol. Soc. Spec. Publ. 42, 313–345. https://doi.org/10.1144/GSL.SP.1989.042.01.19.

Tang, M., Rudnick, R.L., McDonough, W.F., Gaschnig, R.M., Huang, Y., 2015. Europium anomalies constrain the mass of recycled lower continental crust. Geology 43, 703–706. https://doi.org/10.1130/G36641.1.

Tang, M., McDonough, W.F., Ash, R.D., 2017. Europium and strontium anomalies in the MORB source mantle. Geochim. Cosmochim. Acta 197, 132–141. https://doi.org/10.1016/j.gca.2016.10.025.

Tonielli, R., Innangi, S., Di Martino, G., Romagoli, C., 2019. New bathymetry of the Linosa volcanic complex from multibeam systems (Sicily Channel, Mediterranean Sea). J. Maps 15, 611–618. https://doi.org/10.1080/17445647.2019.1642807.

Washington, H.S., 1909. Art. VIII.—the submarine eruptions of 1831 and 1891 near Pantelleria. Amer. J. Sci. 27 (158), 131–150. https://doi.org/10.2475/ajs.s4-27.158.131.

van Westrenen, W., Blundy, J.D., Wood, B.J., 2001. High field strength element/rare earth element fractionation during partial melting in the presence of garnet: Implications for identification of mantle heterogeneities. Geochem. Geophys. 2 (7). https://doi.org/10.1029/2000GC000133.

White, R.S., McKenzie, D., O'Nions, R.K., 1992. Oceanic crustal thickness from seismic measurements and rare earth element inversions. J. Geophys. Res. 97, 19683–19715. https://doi.org/10.1029/92JB01749.

White, J.C., Parker, D.F., Ren, M., 2009. The origin of trachyte and pantellerite from Pantelleria, Italy: insights from major element, trace element, and thermodynamic modelling. J. Volcanol. Geotherm. Res. 179, 33–55. https://doi.org/10.1016/j.volgeores.2008.10.007.

White, J.C., Espejel-García, V.V., Anthony, E.Y., Omenda, P., 2012. Open system evolution of peralkaline trachyte and phonolite from the Suswa volcano, Kenya rift. Lithos 152, 84–104. https://doi.org/10.1016/j.lithos.2012.01.023.

Willbold, M., Stracke, A., 2006. Trace element composition of mantle end-members: implications for recycling of oceanic and upper and lower continental crust. Geochem. Geophys. 7 (4), Q04004. https://doi.org/10.1029/2005GC001005.

Wolff, J.A., 2017. On the syenite-trachyte problem. Geology 45, 1067–1070. https://doi.org/10.1130/G39415.1.

Yang, Z.-F., Zhou, J.-H., 2013. Can we identify source lithology of basalt? Sci. Rep. 3, 1856 (doi: 10/1038/srep01856).

Zindler, A., Hart, S., 1986. Chemical geodynamics. Annu. Rev. Earth Planet. Sci. 14, 493–571. https://doi.org/10.1146/annurev.ea.14.050186.002425.